ISSN 0737-5352
CIRA
Paper No. 1

The Genesis and Development of Deep Convective Storms

Department of Atmospheric Science P.C. Sinclair
NOAA/NESDIS J. F.W. Purdom

CIRA

January 1983

Cooperative Institute for Research in the Atmosphere

Colorado State University
Foothills Campus
Fort Collins, Colorado 80523

Colorado State University / National Oceanic and Atmospheric Administration

TABLE OF CONTENTS

LIST OF FIGURES

ABSTRACT

During the summer of 1980, NESS sponsored a research aircraft field program that combined research aircraft flights with rapid scan GOES imagery. The purpose of the research program was to provide a better understanding of the natural mechanisms that lead to the development of deep convective storms through integration and analysis of those special data sets. Data were taken during the field program with the goal of providing an indepth understanding of the fundamental mechanism - arc cloud line interactions - that lead to the development of deep convection.

The experiment provided a unique data base from which the convective storm's mesoscale flow field (dynamic and thermodynamic properties) could be documented by in-situ measurements and near simultaneous GOES visible and infrared data. Several arc clouds were penetrated on three separate GOES rapid scan imaging days, and representative results from those penetrations are given in the text. It is hoped that the improvement in knowledge gained from this experiment will lead to a better understanding of mesoscale dynamics, which is of great importance for the development of improved short-range forecasting techniques.

I. INTRODUCTION

The convective storm lies at the heart of many weather related events that dramatically effect everyday life. Tornadoes, flash floods, downbursts and severe thunderstorms pose serious threats to life and property throughout the United States. At the same time, portions of the country need summertime precipitation augmentation to improve water resources for human consumption, for power generation, and for agricultural purposes. In addition, military operations such as air refueling, terminal weather forecasting, and air-to-ground support and surveillance can be significantly affected by convective storm development. Although numerical weather prediction models employ various parameterization schemes to enter sub-grid scale feedbacks into the models, one of the major problems these schemes encounter involves the handling of small-scale convection processes. It now seems evident that some of these small-scale processes act as important mechanisms in the chain of events that lead to storm development and evolution.

Understanding the development and evolution of convective storms is one of the most important and challenging problems in meteorology today. While it is generally agreed that the development of a convective storm or storm array depends on the interaction of meteorological fields ranging from the synoptic scale cyclone down to the cloud condensation nuclei (Lilly, 1977), little is known about why a particular storm forms and develops the way it does, or why a convective array behaves in a particular manner. Most of the available information about convective storm development and intensification is focused on either the large-scale conditions favorable for convective development (Miller, 1972), or on the individual convective storm (Brandes, 1978; Browning, 1964;

Fankhauser, 1971, 1976). Indeed, as Simpson and Dennis (1974) point out, more is known about synoptic scale conditions favorable for convective development and cloud microphysics than is known about the mesoscale, which remains virtually unmeasured and unknown: this remains true today.

The lack of information on the intermediate scale (the interaction between convective clouds and their mesoscale environment) has been mainly due to a gap in meteorological observing capability in the days prior to the high resolution geostationary satellite (Purdom, 1976). The geostationary satellite is the only meteorological observing tool that can simultaneously observe the evolution of clouds from the synoptic scale down to the cumulus scale. The clouds and cloud patterns observed in a satellite image represent the integrated effect of ongoing dynamic and thermodynamic processes in the atmosphere. When that information is combined with more conventional data, such as that from research aircraft, the convective scale interactions that are vital to the formation and maintenance of deep convection may be analyzed and better understood (Purdom, 1979; Maddox, 1980).

The National Earth Satellite Service, recognizing the importance of geostationary satellite data in understanding convective development, has operated the GOES system in a special rapid interval imaging mode on selected days during the past several convective seasons (1975-1982). The purpose of that special imaging was to gain insight into the nature of deep convective development as observed with three to five minute interval satellite data. This unique data set allowed, for the first time, observations of convective behavior at temporal and spatial resolutions compatible with the scale of the physical mechanisms

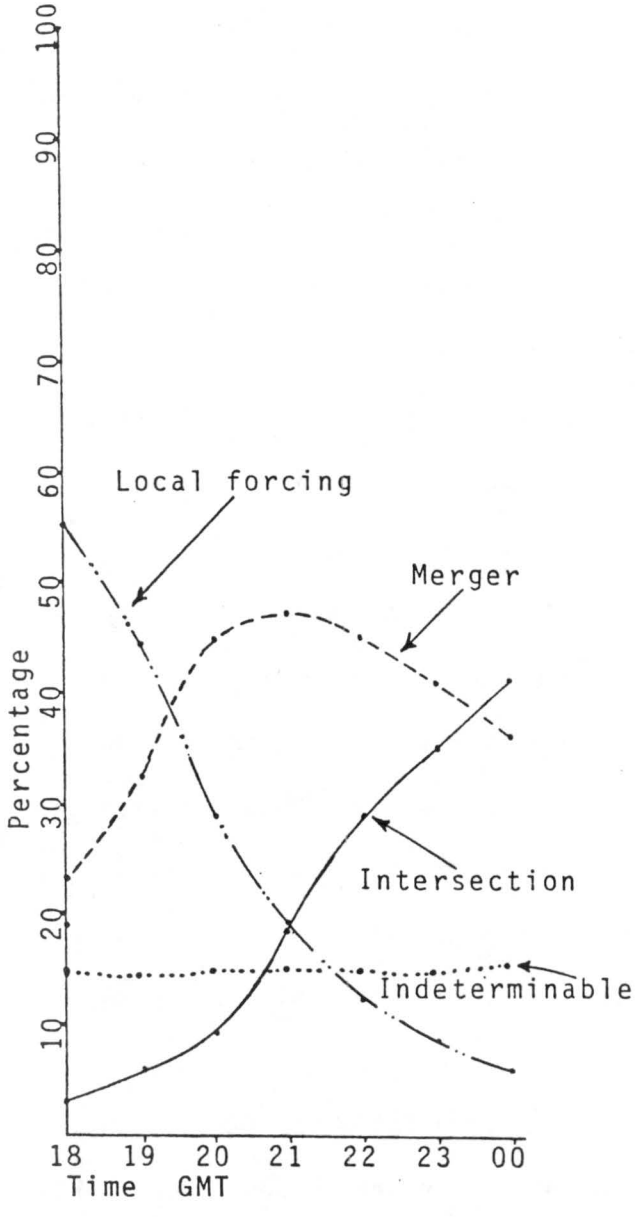

Fig 1a. Distribution of convective generation mechanisms for all storms colder than -20C versus time for the summer of 1979 over the Southeast United States. Sample contains over 9850 storms.

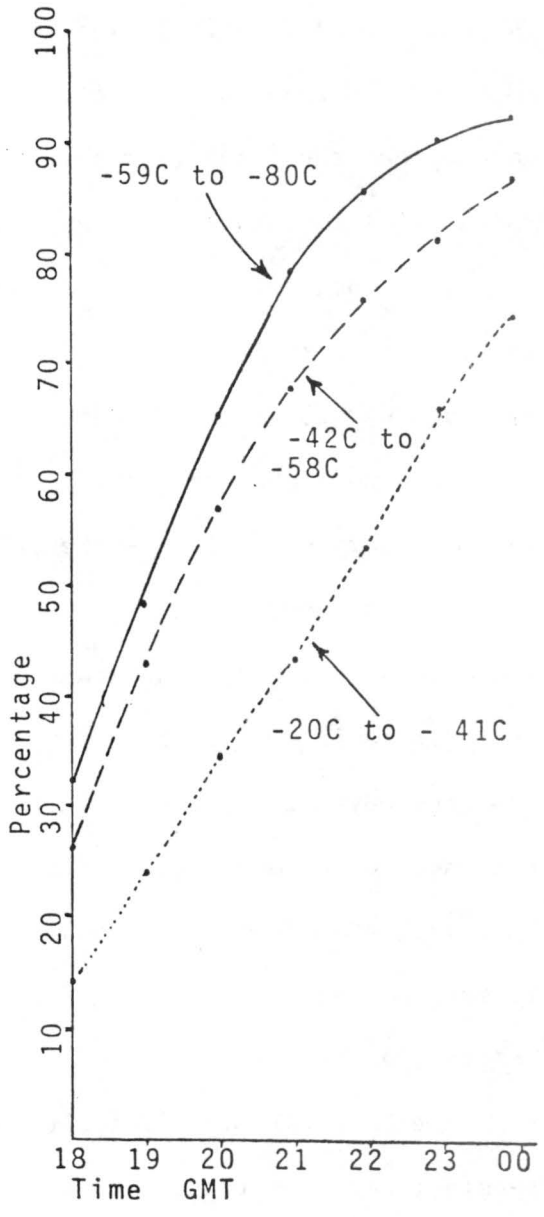

Fig 1b. Percentage of storms in various temperature ranges due to intersections and mergers for a given hour, assuming indeterminable storms in 7a are equally distributed. For example: Of those storms between -59 and -80C at 0000 GMT, 93% are due to merger and intersection.

Figs 1a and 1b, definitions. Merger - storms that form on an arc as it moves into locally unstable air. Intersection - storms that form when two arcs come into contact. Local forcing - storms that form not due to merger or intersection. Indeterminable - those storms whose generation mechanism could not be clearly defined.

responsible for triggering deep and intense convective storms. Movie film strip analysis of those data show that convective scale interaction is of primary importance in determining the evolution of deep convection. This interaction manifests itself as the merger and intersection of thunderstorm produced outflow boundaries with other convective lines, areas, and boundaries (Purdom, 1979, 1982).

In a recently completed study using GOES satellite data, Purdom and Marcus (1982) classified convective development over the southeast United States with respect to storm generation mechanism and intensity. Over 9,850 convective storms were classified for June, July and August 1979 for the six-hour period 1800-0000 GMT (noon to 6:00 p.m. local). Intensity was classified into levels depending on GOES infrared cloud top temperature. Figures 1a and 1b summarize the results for the entire study period. It is important to note that those results show quantitatively for the first time that convective scale interaction, transmitted through arc cloud merger and intersection, is one of the dominant mechanisms responsible for the generation of deep cumulonimbus. Notice that while early in the day local forcing dominates as the main convective generation mechanism, later in the day when the most intense convection has developed the dominant generation mechanisms are due to arc cloud interactions. For the very strongest storms (Figure 1b), the interaction mechanism is clearly all the more important.

The findings of Purdom and Marcus correlate well with those of Simpson (1980) in which she studied downdraft influences on convective development in the near storm environment. In that study, Simpson suggests, "...the cumulus scale downdraft is a crucial element in the chain of events comprising the explosive growth of cumulus clouds, both

natural and seeded, to large cumulonimbus." Arc clouds, which result from thunderstorm downdrafts and outflows (Purdom, 1973), are a natural part of the convective cloud genesis and evolution process. They occur anywhere in the United States and are often the cause of severe thunderstorm development (Purdom, 1976). An extreme example was the severe storm associated with the most destructive tornado in Wyoming history (Parker and Hickey, 1980).

During the summer of 1980, NESS sponsored a research aircraft field program that combined research aircraft flights with rapid scan (3 minute interval) GOES imagery. The purpose of the research program was to provide a better understanding of the natural mechanisms that lead to the development of deep convective storms through integration and analysis of those special data sets. Data were taken during the field program with the goal of providing an indepth understanding of the fundamental mechanism - arc cloud line interactions - that lead to the development of deep convection.

The experiment provided a unique data base from which the convective storm's mesoscale flow field (dynamic and thermodynamic properties) could be documented by in-situ measurements and near simultaneous GOES visible and infrared data. Several arc clouds were penetrated on three separate GOES rapid scan imaging days, and representative results from those penetrations are given in the text that follows. It is hoped that the improvement in knowledge gained from this experiment will help lead to a better understanding of mesoscale dynamics, which is of great importance for the development of improved short-range forecasting techniques.

II. THE EXPERIMENT

2.1 General

The time period available for the experiment meant that the research aircraft flights would have to be made between July 15 and July 22, 1980. For arc-cloud penetrations in a weakly forced atmosphere, the meteorological situation dictated operations along the southeastern Gulf Coast and the northern to central portions of Florida. For a variety of reasons, including logistics, fuel availability, access to weather information and communications, operations were based in north-central Florida. Three days of successful arc cloud penetrations were made: July 17 (near Tampa), July 21 (near Sarasota) and July 22 (near Gainesville), see Figure 3. P.C. Sinclair operated the aircraft (Section 2.2) as pilot/scientist, while J.F.W. Purdom operated the atmospheric data system as observer/scientist.

General areas for penetration were chosen using expert advice from NESS units that had access to real time GOES data (see acknowledgements). Once the aircraft reached an area where arc activity had been detected, decisions concerning penetration points were made visually. Attempts were made to consult the NESS meteorologist using an in-flight phone system at this time; however, reliable communications were unable to be established from the air.

Aircraft position was determined from VOR-DME, LORAN-C, and Doppler navigation systems. At all times the accuracy of aircraft location was well within the resolution of one GOES visible image element (1 Km). Penetrations of the arc cloud region were always made in clear air and below cloud base (generally between 300 and 1000 feet below the cloud).

2.2 Aircraft Observational System

The Colorado State University Atmospheric Research Flight Facility (ARFF) has developed a number of Airborne Atmospheric Data Systems (AADS) for direct measurements of temperature, dew point, pressure, atmospheric constituents and the atmosphere's three dimensional velocity field. These systems have been specially designed for a variety of aircraft for measurements in atmospheric systems ranging in size from mesoscale systems and severe thunderstorms to waterspouts and dust devils (Sinclair, 1973, 1974; Leverson, Sinclair and Golden, 1975). A miniaturization of the AADS system was designed and constructed by the ARFF for the Cessna Turbo 207 aircraft used in this experiment (see Figure 2, pg. 10). It is believed that this is the first installation of this type on a light single engine aircraft (see Appendix A).

Relatively fine structure of the velocity field (u', v' w') is obtained using a gust probe and gyro reference system that is designed to be independent of the aircraft's sensitivity to atmospheric motions and/or pilot induced motions. Temperature and dew point are continuously recorded using a standard Rosemount fast response total temperature sensor and a Cambridge dew point sensor. In addition to the above measurements, a Doppler wind system provides accurate measurements of ground speed and aircraft drift angle. These data, along with aircraft heading and true airspeed provide mean horizontal wind components ($\overline{u}$, $\overline{v}$). Aircraft position data is obtained from VOR/DME and LORAN-C stations along with pressure and radar altimeter instrumentation. Accuracy for measurements of the various parameters mentioned above is given in Table 1, while a more complete description of the Cessna Turbo 207 instrumentation system may be found in Appendix A.

Table 1

Parameter	Relative Accuracy	Absolute Accuracy
Temperature	$0.05^{o}C$	$0.2^{o}C$
Dew Point Temperature	$0.2^{o}C$	$0.5^{o}C$
u', v'	0.1 $msec^{-1}$	0.5 $msec^{-1}$
w'	0.1 $msec^{-1}$	0.5 $msec^{-1}$
$\bar{u}$, $\bar{v}$	0.5 $msec^{-1}$	1.0 $msec^{-1}$
a/c location	±0.1 nm	±0.2 nm

2.3 GOES Data

For each of the case study days, nominal 3 minute interval GOES-East imagery were taken during the flight periods. The scheduling for the 3 minute interval imaging was the same as was used in SESAME Operations (Barnes, 1981). The 3 minute images covered the study area very well; and, in all cases, sufficient landmarks were available to insure aircraft and satellite cloud locations to within the resolution of the GOES image. Analysis of the rapid scan satellite data versus aircraft locations leave no doubt that the aircraft measurements represent, for the first time, continuous data sets through the arc cloud lines in the sub-cloud region.

Figure 2. Cessna Turbo 207 Atmospheric Research Aircraft.

The Cessna T207 aircraft is the largest single-engine light plane manufactured in the U.S. and consequently it provides maximum volume and payload capabilities at minimum cost. The aircraft is STOL equipped for high accuracy wind and gust measurements and isokinetic air sampling requirements. The gust probe system is mounted in a pod under the left wing and a doppler navigation - wind system is located in a specially designed pod located on the bottom of the fuselage near the tail of the aircraft.

A fast response total temperature sensor is shown mounted on the upper part of the vertical plate on the right wingtip. On the lower part of the plate, a special splitter plate mount houses the Cambridge dew point sensor. The splitter plate provides unobstructed flow past the sensor air ports. The temperature and dew point sensors are mounted on the wing-tip to minimize engine effects and contamination and adverse airflow situations at other wing-fuselage locations.

N8102S

III. MEASUREMENTS AND OBSERVATIONS

Arc cloud lines were penetrated on three separate case study days: July 17, 21 and 22, 1980. The penetration regions of the arc cloud lines for each of these days, as well as the aircraft penetration ground tracks are shown in Figure 3. A description of each of the flight measurement days follows.

3.1. 21 July 1980

The main penetration area of the arc cloud line was located on approximately the 35 degree VOR radial between 39-53 km from Saraosta, Florida (see Figure 3). The width of the arc line, about 14 km, is shown by the hatched-line region in Figure 3, with the arrow depicting the aircraft path for the 2027 GMT penetration. Multiple transverses were made of the arc region on this day at an altitude of 1037 msl (1000 AGL), which was approximately 150 m below cloud base.

Figures 4a and 4b (pg. 13) are GOES-East, 1 km resolution visible images taken near the beginning and ending times of the penetrations that were made on 21 July. On this day, early shower activity in central Florida, to the east of Sarasota, produced an arc cloud line region that moved westward over the area of interest by midday. The considerable westward displacement of the arc region is due in part to the strong low-level easterly flow across Florida: notice for example the long downstream clear area to the west of Lake Okeechobee.

Figure 4c* is a mesoscale analysis based on the cloud patterns shown

*Nephanalyses of this type are included to show arc locations. Arc identification from a single photograph is often extremely difficult and requires movie loop analysis for positive identification. This nephanalysis, and those that follow, were based on movie loop interpretations of the 3 minute interval imagery.

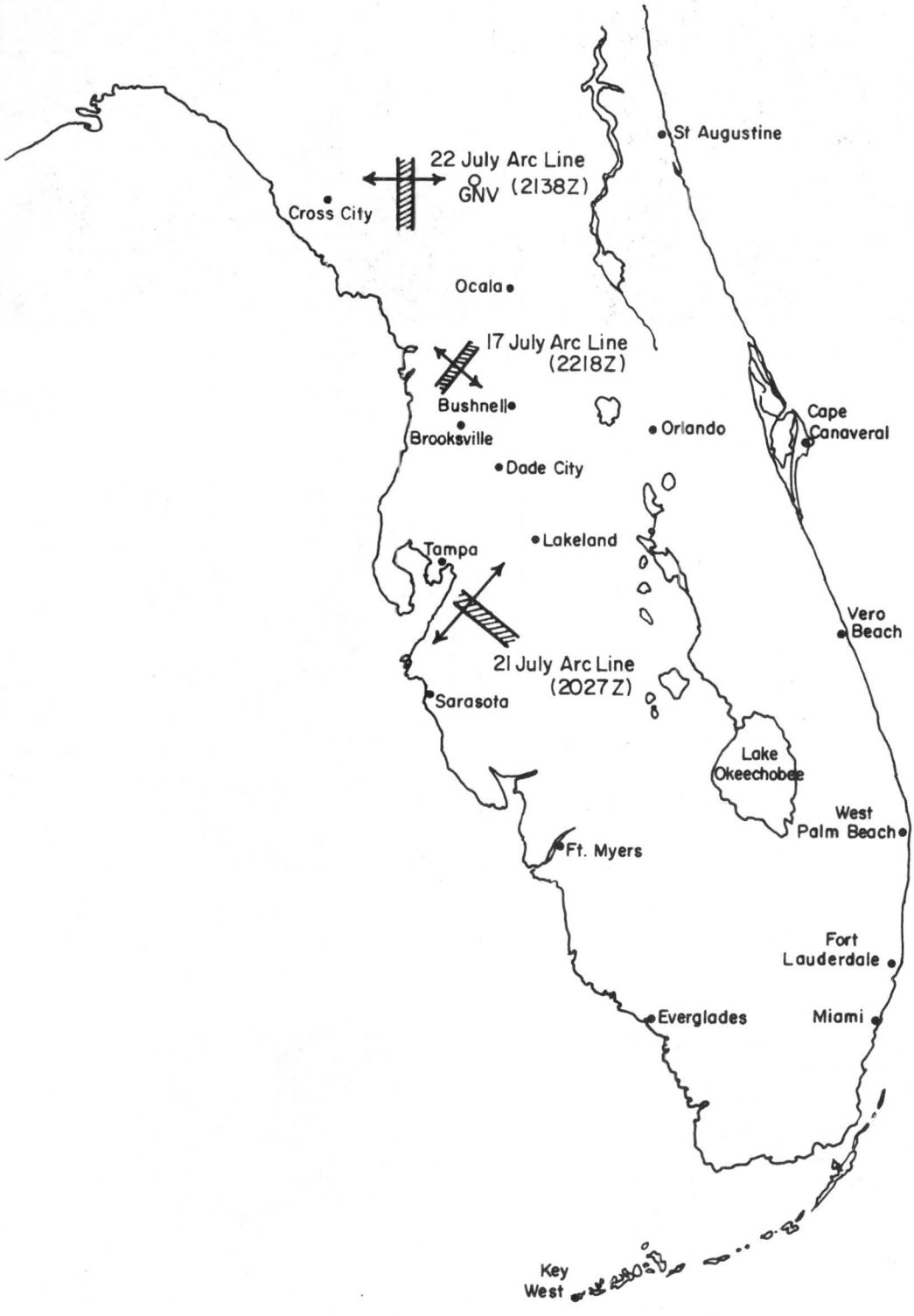

Figure 3: Cloud Arc-Line Locations.

The cloud arc-lines are depicted by the hatched-line areas. The aircraft penetration directions and the ground tracks are shown by the arrows through the hatched areas. The mean penetration times are shown below the penetration dates.

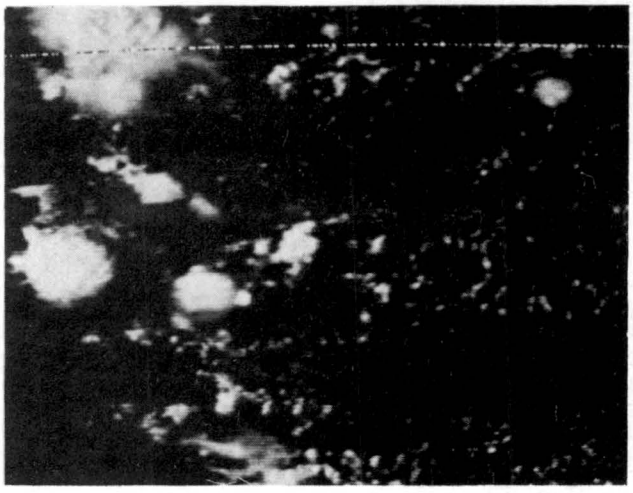

Fig 4a. 21 July 1980 at 2030 GMT. GOES-East 1Km resolution visible image. Analysis in Fig 4c below.

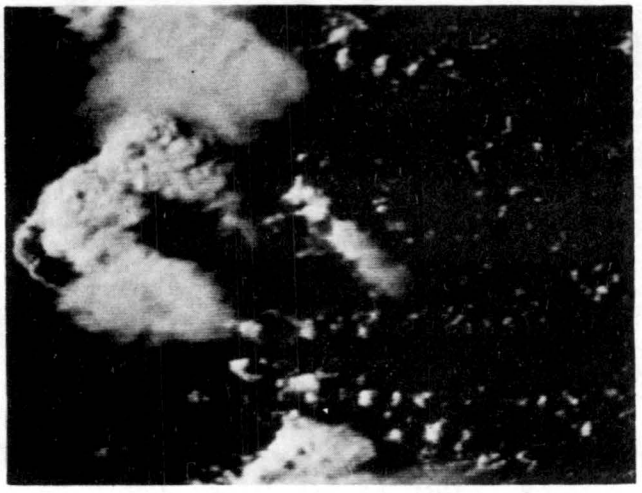

Fig 4b. 21 July 1980 at 2144 GMT. GOES-East 1Km resolution visible image. Analysis in Fig 4d below.

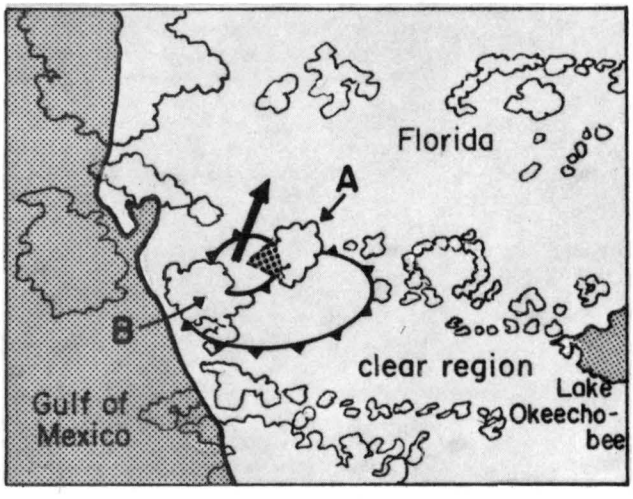

Fig 4c. Nephanalysis of Fig 4a. Arrow shows flight path, shaded area gives view for Fig 4e below.

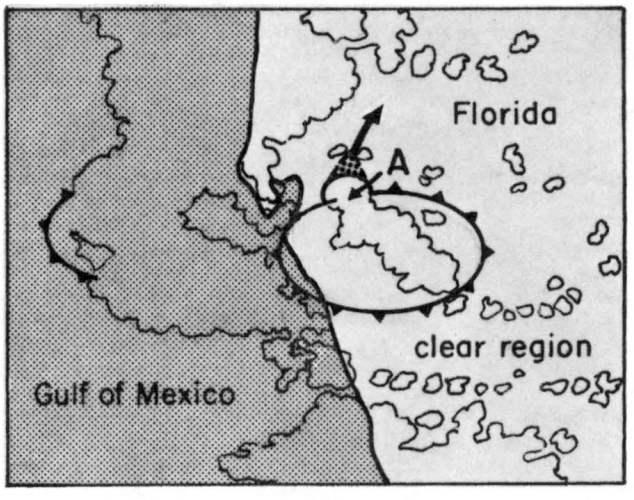

Fig 4d. Nephanalysis of Fig. 4b. Arrow shows flight path, shaded area gives view for Fig 4f below.

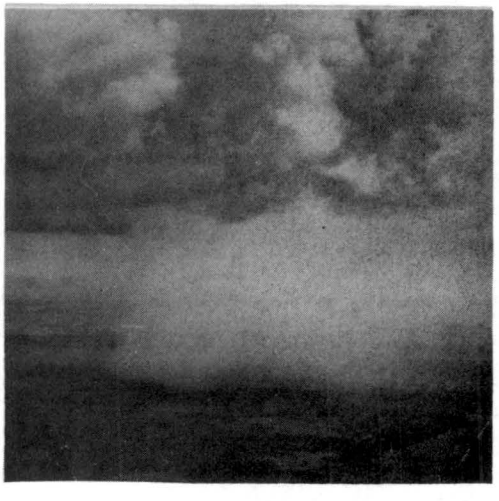

Fig 4e. Photograph of cloud A (Fig 4c) at 2021 GMT prior to penetration of arc.

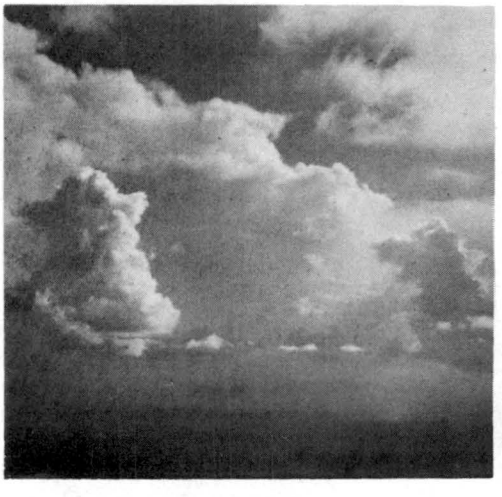

Fig 4f. Photograph of cloud A (Fig 4d) taken at 2151 after final arc penetration.

in Figure 4a. In Figure 4c, notice that two areas of stronger convection are evident along the arc at points A and B. Additionally a smaller arc, due to earlier convection that had dissipated, is apparent along the arc between the stronger convection at A and B. The photograph shown in Figure 4e was taken from the aircraft prior to our initial penetration of the arc along the arrow shown in Figure 4c. The cloud shown in the photograph (Figure 4e) is of cloud A in Figures 4a and 4c: notice the rain shower evident beneath that cloud. We believe that the replenishment of negatively buoyant air into the boundary layer by showers such as the ones at A and B, as well as the one that produced the small arc between A and B, is one of the major factors that enables arc cloud lines to maintain their identity for periods of up to several hours in some cases.

Figure 4d is a mesoscale analysis based on the cloud patterns shown in Figure 4b.* This GOES-East image was taken approximately 12 minutes after our final penetration of the day, as was the aircraft photograph shown in Figure 4f, which was taken looking back to the south at the arc cloud line. An interesting feature is that storm A continued to regenerate along the northern portion of the arc: note the shower activity evident in Figure 4f. In Figure 4f, also note the small line of non-precipitating cumulus ahead of the main shower, which again suggests the importance of the precipitation/evaporation process to the continuous regeneration of convective clouds along arc cloud lines.

*An interesting feature shown in this GOES image is the strong thunderstorm activity and the arc cloud line to the west of Sarasota over the Gulf of Mexico. This is not related to storm B, but rather with the shower that moved off-shore as seen in Figure 4a.

Table 2

Variable	Maximum Variation from Mean Environment
T	$\pm 0.6^{o}C$
T_d	$+1.2^{o}C$ to $- 0.9^{o}C$
w	+3.6m/sec to - 2.4m/sec

Aircraft measurements from a penetration centered on 2027 GMT, Figure 5, are typical of those taken on this day. In Figure 5, the distribution of temperature (T), moisture in the form of dew point temperature (T_d), and vertical motion (w) are shown with respect to their mean environmental values during the arc cloud line traverse. The warm, moist core of the updraft region is typical of most arc cloud line penetrations above the outflow frontal zone (see Figure 10 for schematic of outflow frontal zone). The maximum variations of T, T_d and w from their mean environmental values ($\overline{T}_e$, $\overline{T}_{de}$, $\overline{w} = 0$) are shown in Table 2. Notice that the vertical motion field below cloud base is strongly positive, while descending motion on either side of the main updraft is also evident. This descending motion, a type of return flow circulation, is also a prominent feature along the boundaries of dry thermals, cumulus clouds, and severe storms (Sinclair, 1973). This descending sheath of air appears to have its maximum values in close proximity to the updraft core with lower values at larger radii in the environment as depicted in Figure 5.

In this case, the return circulation around the updraft appears slightly cooler than the mean environmental temperature ($\overline{T}_e$). The warm, moist air of the arc line updraft region has its origin in the surface

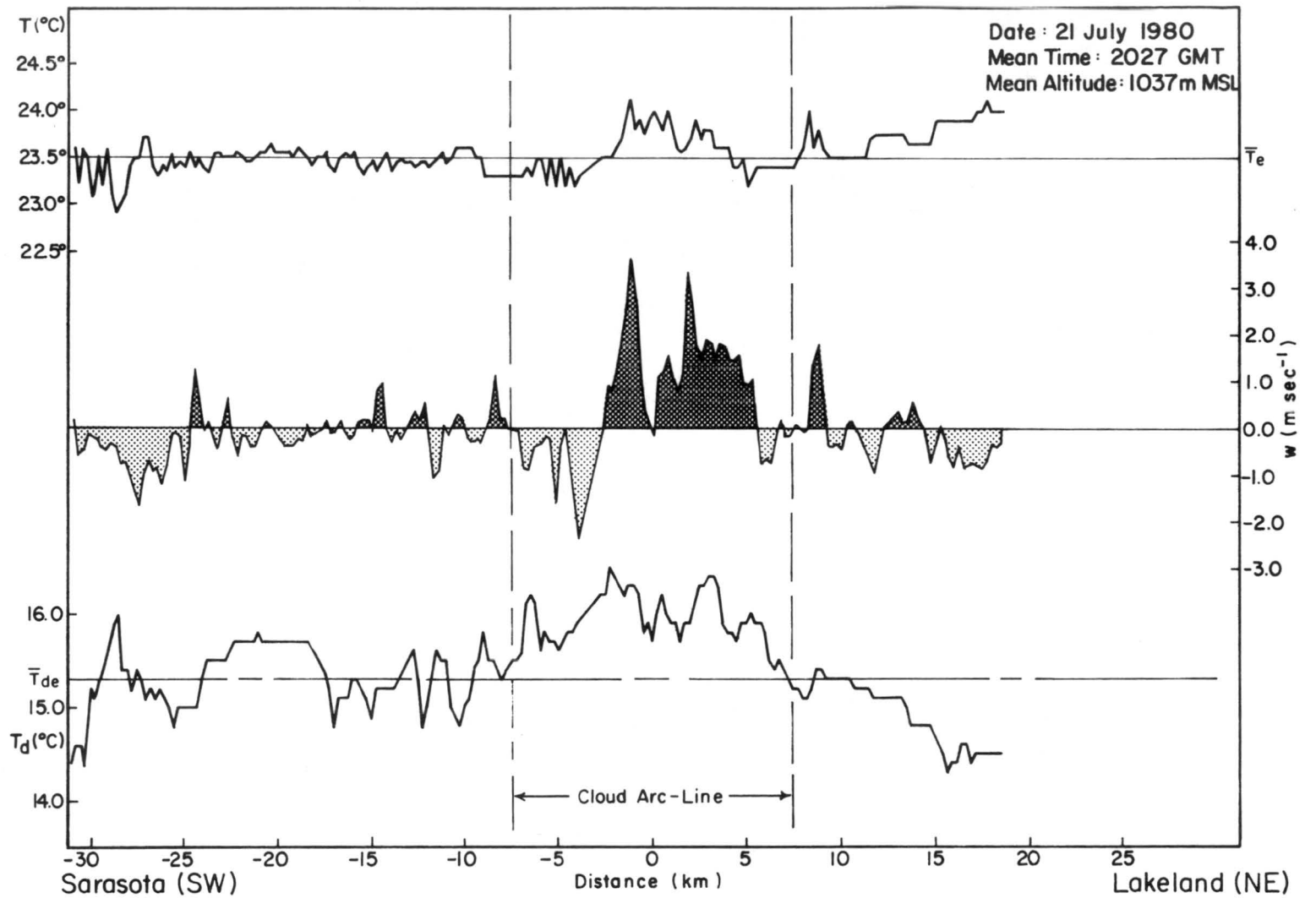

Figure 5. Aircraft Data of Arc Line Penetration for 21 July 1980, 2027 GMT.

The distribution of temperature (T), dew point (T_d), and vertical motion (w) are shown with respect to their mean environmental values: $\overline{T}_e$, $\overline{T}_{de}$, and w=o. The lateral boundaries of the cloud arc line are indicated by the dashed vertical lines at ± 7 km from the arc centerline.

boundary layer ahead of the advancing arc line frontal zone. As previously shown, some of the clouds along the arc line had progressed to the precipitation stage by the time of the penetration (2.5 to 6.5 km interval; Figure 5), light showers were penetrated before exiting to the clear zone on the NE side of the arc line. In the precipitation areas the vertical motion was both positive and negative, with evaporative cooling causing the temperature to be slightly below ambient (T_a) and the increase in moisture.

3.2. 22 July 1980

On this day an outflow boundary which was located approximately 38 km to the west of Gainesville was formed by shower and thunderstorm activity along Florida's west coast sea breeze frontal zone. The main area of penetration is shown in Figure 3, with the arc cloud line region depicted by the hatched region and the arrow depicting the aircraft path for the penetrations. In order to obtain data at different levels below the cumulus along the arc cloud line, three sub-cloud penetrations were made at altitudes of 480 m, 800 m, and 1067 m MSL (terrain elevation in this area is approximately 15-30 m).

Figure 6a is a GOES-East, 1 km resolution visible image centered near the time of the arc cloud line penetrations. On this day, shower and thunderstorm activity along Florida's west coast sea breeze front produced an array of arc cloud lines, some of which are detectable in Figures 6a and 6b. Figures 6c and 6d are mesoscale analyses based on the cloud patterns shown in Figures 6a and 6b, as well as their evolution as revealed in rapid scan GOES imagery. Note the large thunderstorms at A, B and C in Figure 6b. These storms developed where arc cloud line #2 intersected three nearby discontinuities, i.e.: (1) arc cloud #3

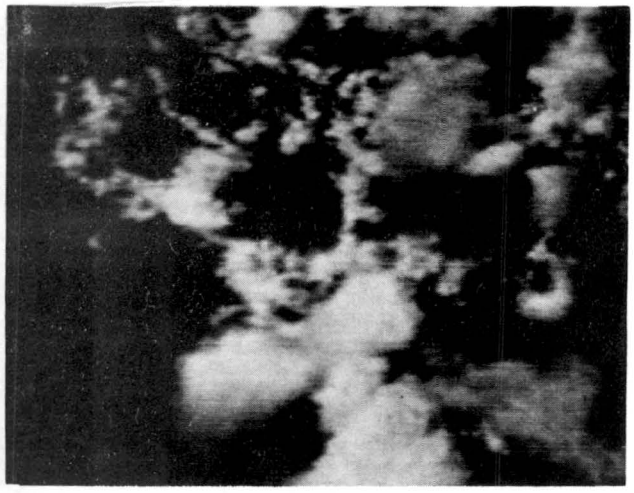

Fig 6a. 22 July 1980 at 2030 GMT.
GOES-East 1 Km resolution visible image.

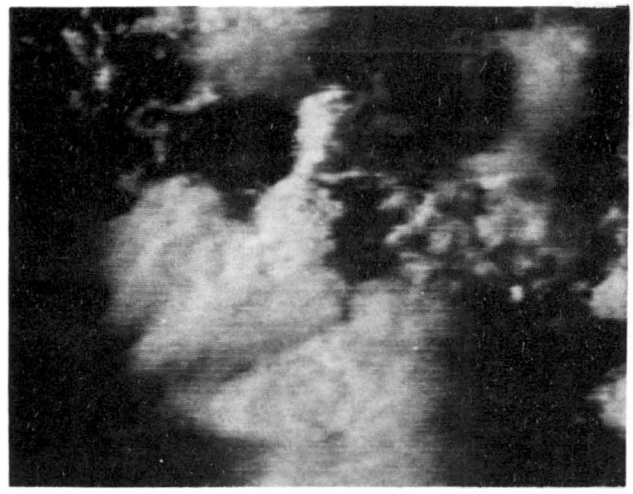

Fig 6b. 22 July 1980 at 2144 GMT.
GOES-East 1 Km resolution visible image.

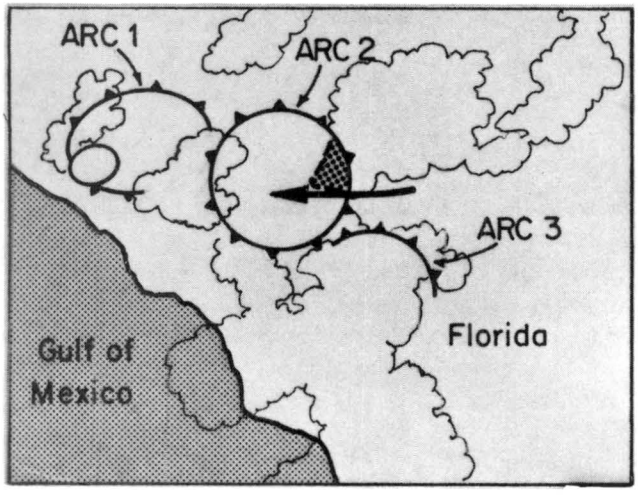

Fig 6c. Nephanalysis of Fig 6a. Arrow shows flight path, shaded area gives field of view for montage in Fig 6e.

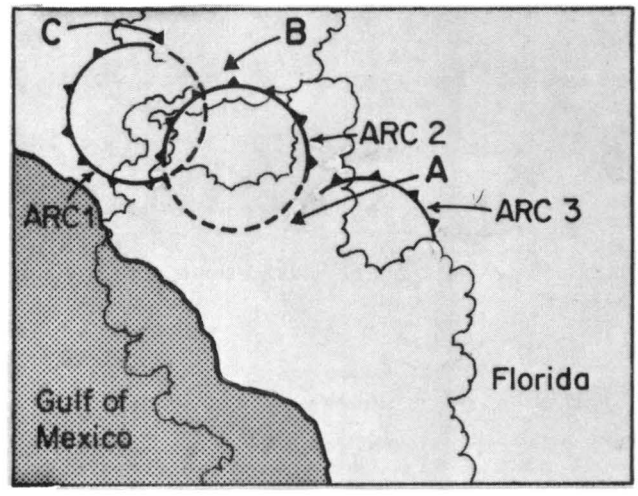

Fig 6d. Nephanalysis of Fig 6b. Note the large thunderstorms that have formed due to arc 2's various interactions (see text).

Fig 6e. Montage of arc cloud region, taken from its interior after the initial penetration. See Fig 6c.

(thunderstorm A); (2) arc cloud #1 (thunderstorm C); and (3) the convective region to its north (thunderstorm B). Penetration activity was confined to the eastern portion of arc #2 (flight track arrow in Figure 6c). This arc was the youngest and most vigorous of the arcs penetrated on the three experiment days.

The montage in Figure 6e shows the congestus along the eastern side of the arc immediately after our initial east-to-west penetration: notice the clearer skies above (also evident in Figures 6a and 6b) as well as the shower activity along the arc. The importance of shower activity in the production of negatively buoyant air in the sub-cloud region was mentioned in the discussion of the previous case (21 July). Horizontal divergence of the relatively cool, low-level, arc cloud air mass promotes sinking of the air above it and the resultant clearing.

At all three levels of penetration, the region above the surface outflow boundary was characterized by a warm updraft core which extends upward to cloud base at 1250 m. The measurement profiles of T, T_d and w are shown in Figure 7. Within the updraft region, the maximum variations of T, T_d and w were similar to that found in the 21 July case (compare Tables 2 and 3).

Table 3. Arc-line Penetration Parameter Values

z (m)	$\bar{T}$ (^{o}C)	$\overline{\Delta T}$ (^{o}C)	ΔT_{max} (^{o}C)	γ_p $^{o}C/100m$	$\bar{T}_d$ (^{o}C)	$\overline{\Delta T}_d$ (^{o}C)	$\Delta T_{d_{max}}$ (^{o}C)	Δw ($msec^{-1}$)
480	28.8	1.6	1.9	1.00	16.4	0.4	-0.7	3.1
800	25.6	0.9	1.3	1.05	15.8	0.2	-1.3	2.4
1067	22.8	0.3	0.6		15.3	0.3	-1.1	2.6

In Table 3 the various parameters have the following meanings:

$z \equiv$ altitude (MSL)

$\bar{T} \equiv$ updraft mean temperature

$\overline{\Delta T} \equiv \bar{T} - \bar{T}_e$ ($\bar{T}_e \equiv$ mean environmental temperature)

$\Delta T_{max} \equiv T_{max} - \bar{T}_e$ ($T_{max} \equiv$ maximum updraft temperature)

$\gamma_p \equiv$ process lapse rate

$\bar{T}_d \equiv$ updraft mean dew point

$\Delta \bar{T}_d \equiv \bar{T}_d - \bar{T}_{de}$ (mean environmental dew point)

$\Delta T_{d_{max}} \equiv T_{d_{min}} - \bar{T}_{de}$ ($T_{d_{min}} \equiv$ updraft minimum dew point)

$\Delta w \equiv$ updraft maximum velocity excess.

Figure 7. Aircraft Data of Arc Line Penetrations for 22 July 1980, 2023-2049 GMT.

The distribution of temperature (T), dew point (T_d), and vertical motion are shown for three separate levels ($\bar{z}$=480 m, 800 m, and 1067 m MSL) with respect to their mean environmental values: $\overline{T}_e$, $\overline{T}_{de}$, and w = o. The extent of the lateral boundaries of the cloud arc line are indicated below the temperature profiles.

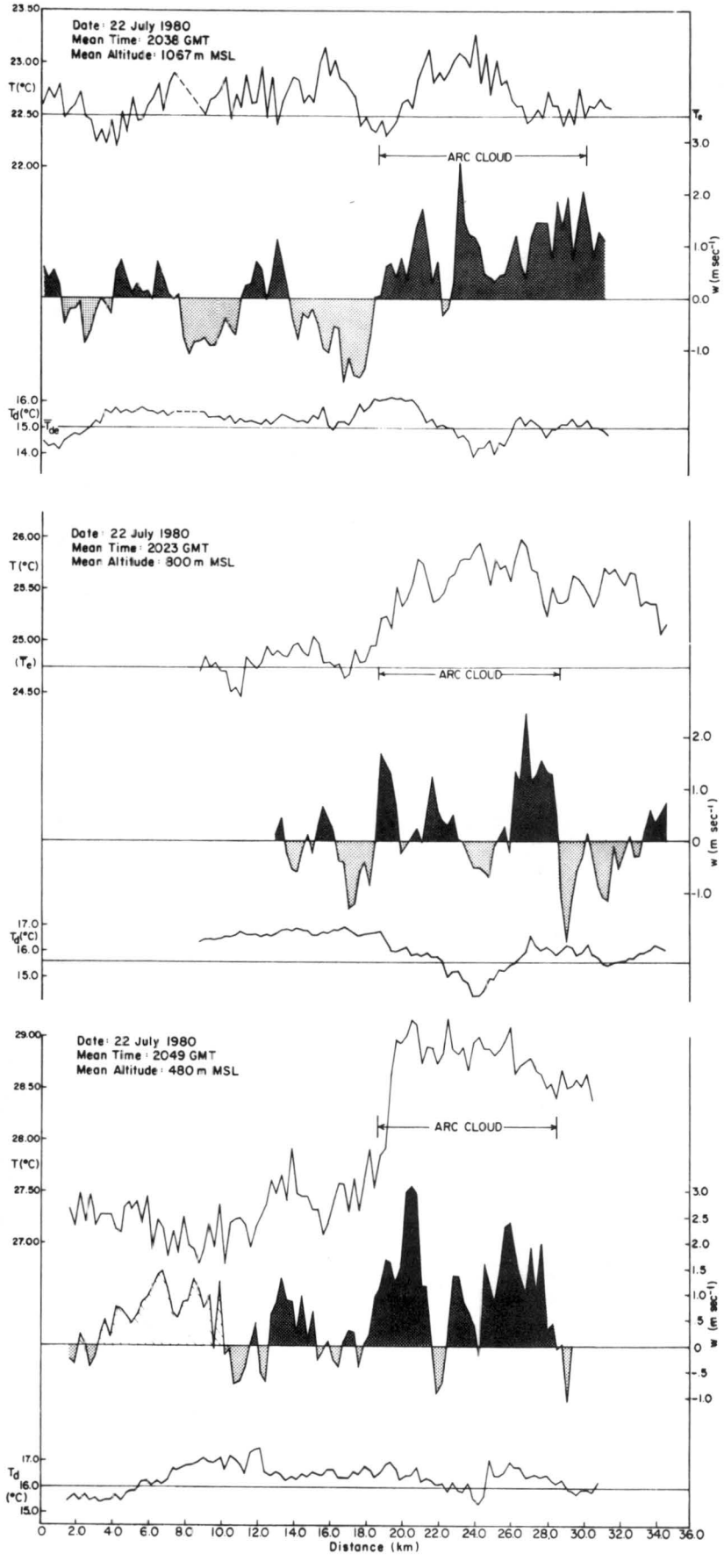
Date: 22 July 1980
Mean Time: 2038 GMT
Mean Altitude: 1067 m MSL
T(°C)
ARC CLOUD
w (m sec⁻¹)
Td(°C)
Date: 22 July 1980
Mean Time: 2023 GMT
Mean Altitude: 800 m MSL
T(°C)
ARC CLOUD
w (m sec⁻¹)
Td(°C)
Date: 22 July 1980
Mean Time: 2049 GMT
Mean Altitude: 480 m MSL
T(°C)
ARC CLOUD
w (m sec⁻¹)
Td (°C)
0 2.0 4.0 6.0 8.0 10.0 12.0 14.0 16.0 18.0 20.0 22.0 24.0 26.0 28.0 30.0 32.0 34.0 36.0
Distance (km)

Important features of these multiple level, arc line penetrations are summarized below (refer to Figure 7).

(1) A pronounced warm, updraft region is evident below the arc cloud line at all levels (480-1067 m MSL). Both $\Delta\overline{T}$ and ΔT_{max} indicate a temperature excess range of approximately $0.5^{o}C$ to $2.0^{o}C$. Mixing of cooler environmental air into the arc line updraft region is in part responsible for the $\gamma_p > \gamma_{dry}$ and the decrease of $\Delta\overline{T}$ and ΔT_{max} with height. The ratio of environmental air to updraft air (by mass percent) involved in this mixing varies from approximately 12% (480 m - 800 m) to 67% (800 m - 1067 m). Greater mixing in the 800 m - 1067 m layer is required to account for the close approach of the updraft mean mixture temperature ($\overline{T}_m$) to the mean temperature of the environment ($\overline{T}_e$). The mixing calculation is based on a calorimetric mixture of the (mean) updraft and environmental air for a "sawtooth" approximation* to the process lapse rate (γ_p), i.e., at the mixing level the mean heat content of the mixture ($M_m Cp_m \overline{T}_m$) is equal to the mean heat content of the updraft air below the mixing level ($M_u Cp_u \overline{T}_u$) and the environmental air ($M_e Cp_e \overline{T}_e$) mixed into the updraft air:

$$M_m Cp_m \overline{T}_m = M_e Cp_e \overline{T}_e + M_u Cp_u \overline{T}_u,$$

where $\overline{T}_e$ = mean environmental temperature, $\overline{T}_u$ = mean updraft temperature M_m, M_e and M_u are the mean mixture, environmental and updraft air masses, respectively. Since specific heats (Cp_m, Cp_e, Cp_u) are essentially

*A sawtooth approximation involves a dry adiabatic ascent of the updraft air over a small vertical distance such that the mixing of mean updraft quantities with its environment takes place at the end of each adiabatic increment. The end points of a series of these sawtooth approximations describe the process lapse rate (γ_p).

equivalent here, the mean mixing ratio of the environmental air to the updraft air is given by:

$$\frac{M_e}{M_u} = \frac{\overline{T}_u - \overline{T}_m}{\overline{T}_m - \overline{T}_e}$$

(2) The peak updraft velocity, like the temperature excess, shows a general decrease in magnitude with height. Thus as the buoyancy driving force decreases with altitude, the vertical motion field follows in step until cloud base is reach where additional buoyancy is generated through the release of latent heat.

(3) Descending motion around the main updraft region is apparent only at the upper penetration level (1067) which is approximately 150 m below cloud base. Here a somewhat warmer recirculating downward flow near the cloud lateral boundaries is apparent at the forward edge of the arc cloud line where the vertical velocities decrease to w = -1.5 m sec^{-1}. At the lower levels this recirculating flow is not so apparent.

(4) At the 480 m penetration level, the vertical motion, temperature and moisture measurements suggest negatively buoyant thermals in the interval 14 to 21 km ahead of the arc cloud line main updraft (cross-hatched w profile). These cool ($\Delta T = -0.5^{o}C$), moist upward thrusts of surface boundary layer air represent the tops of overshooting thermals that because of their size and organization have been sufficiently mixed with the environment to reach a density equilibrium level below 480 m. This point will be discussed further in the Section IV.

(5) Probably the most intriguing feature of these arc line measurements is shown by the moisture distribution in the updraft region at all three levels. In all cases, the dew points decrease dramatically as the center of the updraft is approached. The maximum dew point deficiencies ($\Delta T_{d_{max}} = T_{de_{min}} - \overline{T}_d$) for each penetration are shown in Table 3. This somewhat drier air is flanked by moist air that has risen from lower levels in the marine boundary layer ahead of the arc line outflow. The presence of the relatively dry updraft core region raises the following questions:

1) What is the source of the drier air?

2) Why is the drier air imbedded in the core of the updraft rather than along the updraft flanks?

The most plausible source of the drier air is the relatively cool, dry air of the outflow. It is hypothesized that the presence of this slightly drier air in the updraft is a result of the mixing of relatively cool, dry outflow air with the warm, moist marine air ahead of the outflow frontal zone or density surge line (DSL). Since our aircraft flights were too high for penetration of the DSL, this mixing hypothesis is based on data and results from meteorological tower and experimental tank measurements of gravity currents. Tank experiments of gravity currents (Keulegan, 1957, 1958; Middleton, 1966; Simpson, 1969, 1972) indicate that the DSL surface geometry contains numerous clefts and lobes indicating mixing of the two fluids. For example, this cleft and lobe structure is clearly shown at the leading edge of a laboratory gravity current outflow experiment in Figure 8. Environmental fluid (in this case water) in the boundary layer is drawn into the clefts which results in a mixed fluid within the lobes. Simpson (1972) indicates that "the

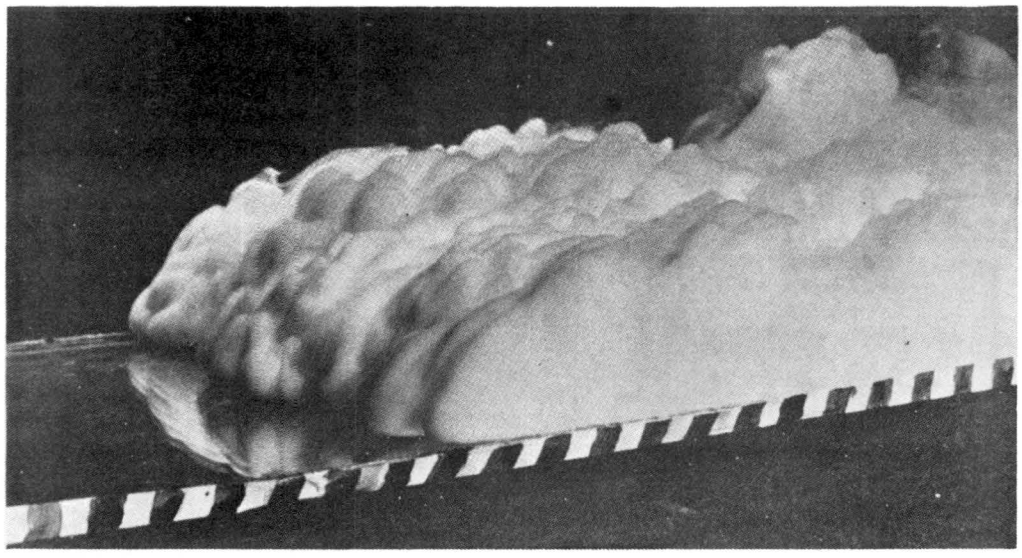

Figure 8: A saline solution (moving right to left) of a laboratory tank experiment (Simpson 1969) shows the similar cleft and lobe structure observed in several gravity type current flows in the atmosphere.

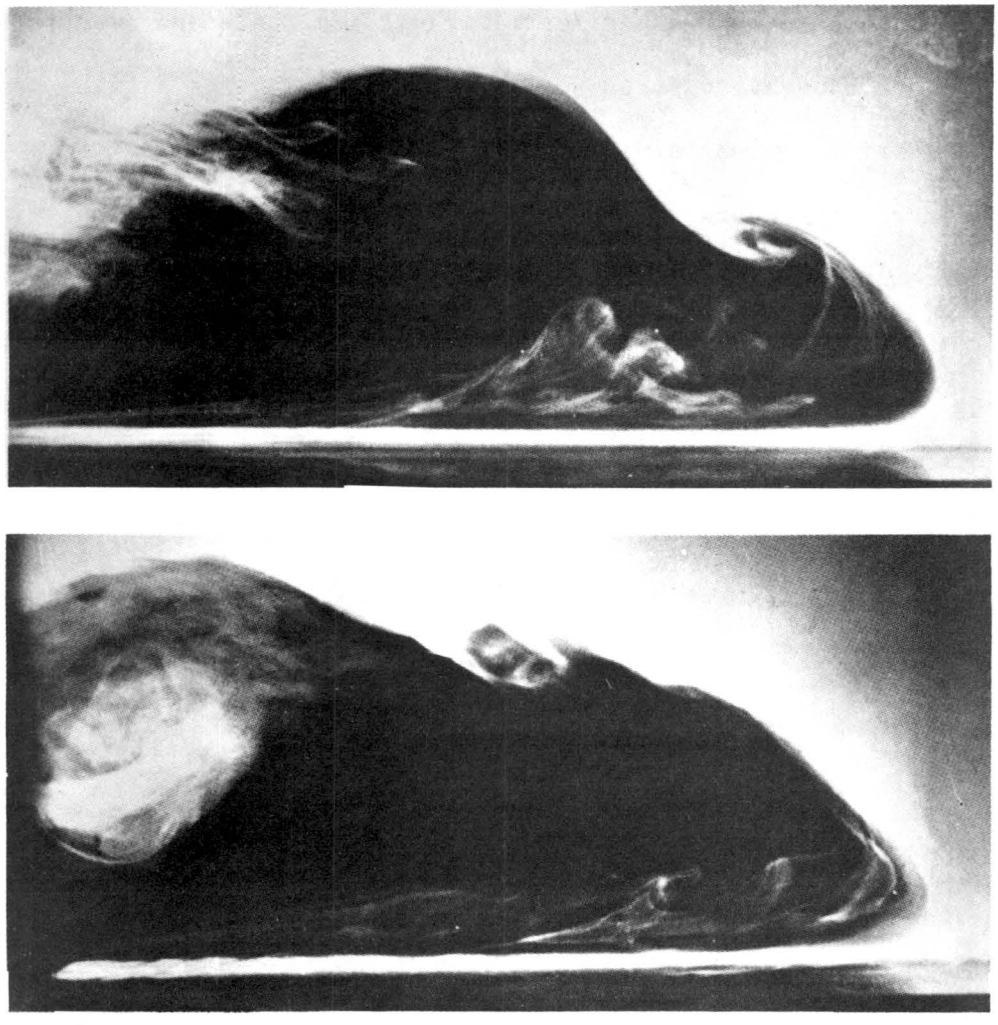

Figure 9: Patches of lighter fluid trapped below the dark, advancing laboratory gravity current are mixed into the base of the head and then swept toward the nose of the outflow (moving to the right).(Simpson 1972)

extent of the penetration of unmixed fluid in the cleft is of the same order as the lobe size". These tank experiments clearly show the mixing of trapped boundary layer fluid with the gravity current outflow (Figure 9).

The leading edge of the gravity current flows simulated in the tank experiments has a structure which appears similar to the leading edge structure of haboobs (Delsi, 1968; Idso, 1972; Lawson, 1971), seabreeze fronts (Simpson, 1969), and dry cold fronts (Martin, 1973). Instrumented tower measurements show that the squall-line gust front may also exhibit similar DSL morphology and fluid mixing characteristics (Charba, 1974; Goff, 1976). Thus, both experimental gravity currents and severe types of atmospheric gravity flows suggest that the arc line outflow may also be modified by turbulent mixing at the DSL interface. As vividly shown in the tank experiments of Simpson (1972), similar mixing of warm, moist air with relatively cool, dry air on either side of the arc-line DSL would result in a lower moisture content of the updraft. It is important to note that while the temperature or sensible heat content of the updraft air ahead of the DSL is also reduced by mixing with the cool air behind the DSL, the lifting and mixing of a superadiabatic layer below the outflow dome apparently results in an updraft mixture that is still warmer (and also drier) than the surrounding environment. These features and processes are schematically illustrated in Figure 10. Mechanical lifting of the relatively warm, moist environmental air (ρ_1) by the leading edge of the storm's outflow (ρ_2) leads to the development of a warm buoyant updraft above the DSL. Because of frictional effects in the lower boundary, the nose of the DSL overrides a thin layer (hatched lines) of warm, moist environmental air.

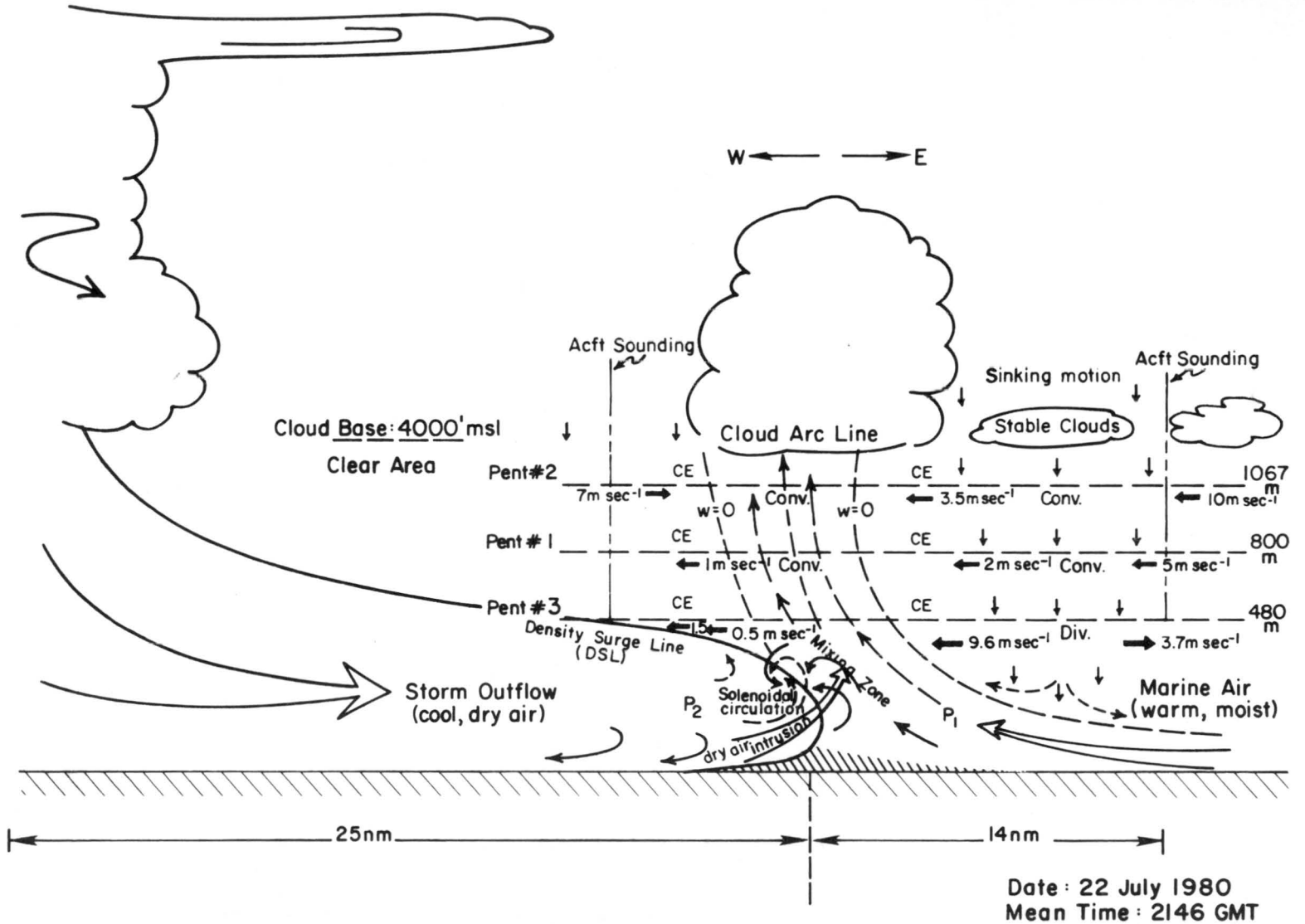

Figure 10. Schematic Illustration of the Cloud Arc Line Features.

The cloud arc line is formed above the leading edge of the density surge line (DSL). Dry air intrusion takes place in the mixing zone at the leading edge of the DSL. The environmental flow field provides a net convergence around the main updraft region.

The unstable layer that then develops below the nose of the outflow promotes vigorous mixing and vertical motions which penetrates into the lower DSL nose region. Additional mixing may also take place in the cleft regions between the nose lobe structure and in the solenoidal circulation ($-\nabla\alpha x\nabla p$) that develops from the strong isosteric/isobaric gradients that exist in the leading edge of the DSL. This mixed, but still buoyant, air may enter the main updraft that feeds the cloud arc-line above the DSL. The more extensive the mixing between the two air masses, the greater the probability of finding relatively dry air within the main updraft. Consequently, the more intense and/or rapidly moving thunderstorm outflows should exhibit these features.

The answer to the second question concerning the location of the relatively dry air within the updraft core can perhaps be answered as follows. Initially, the low level air is spread across a large part of the main updraft. However, as the buoyant updraft penetrates to higher levels, mixing with the environment takes place. This environmental air is more moist than the low level mixed air and, thereby, acts to maintain a relatively moist updraft boundary around the drier updraft core as seen in the measurements (Figure 7). The Doppler wind components along the aircraft flight path are also depicted at each penetration level in Figure 10. The general field of convergence in the environment around the updraft above the DSL suggests that both the mean and turbulent flow fields act to modify the updraft boundaries ($w = o$) with relatively warm, moist environmental air. The horizontal wind components (Figure 10) also suggest a weak convergent-divergent flow field near and within the sub-cloud region surrounding the main updraft. The general sinking motion depicted for this region is also in agreement with the stable clouds or

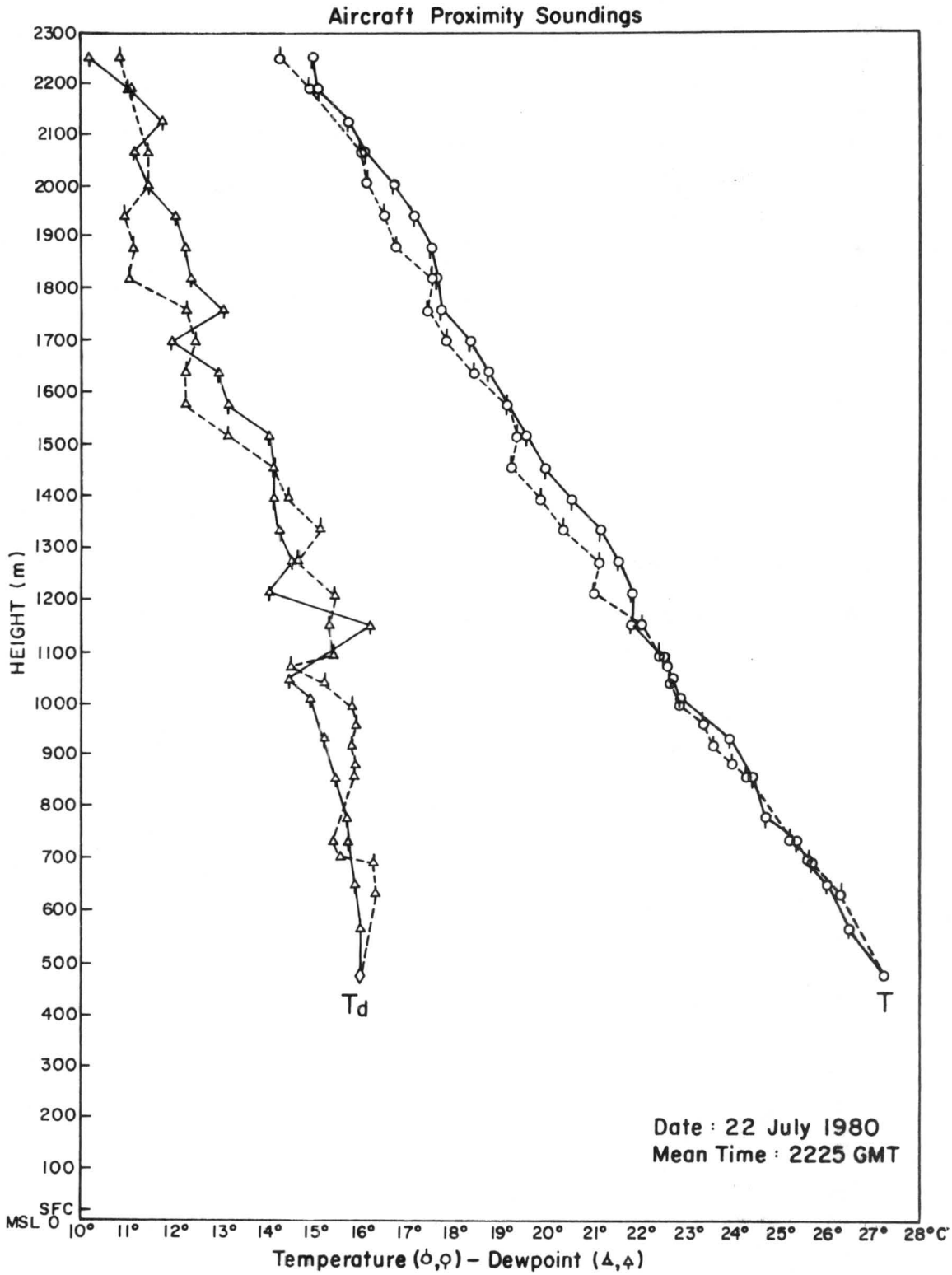

Figure 11. Aircraft Proximity Soundings.

See text for definition and explanation of temperature-dew point ascent (♂ - △) and descent (♀ - ▽) terminology.

clear regions on both sides of the arc-line cloud. The vertical structure of the environment on either side of the arc-line cloud (Figure 10) is shown in Figure 11. The aircraft sounding (♀,♀) taken to the east of the arc line was obtained during a slow descent while that to the west of the arc line represents measurements during a continuous climb (♂,♂) from approximately 1500 feet to 7500 feet MSL. The climb-descent proximity soundings indicate that the unmodified marine environment within this layer (1500-7500 feet) and in close proximity to the arc-line cloud has little variation in the upwind/downwind directions over the storm outflow region. At best, the east descent profile appears slightly warmer and more moist than the west ascent profile. Both soundings indicate a near neutral layer between 1500 feet to 3000 feet.

3.3. 17 July 1980

In this particular case, the arc cloud line penetrated was nearly 6 hours old and had a weak, rather ill-defined high cloud base on its northern boundaries. The arc line was penetrated at an altitude of 1070 m in a NW to SE direction north of Tampa, near the Town of Bushnell, Florida (see Figure 3).

Figures 12a and 12b are GOES-East, 1 km resolution visible images taken 1 1/2 hours apart. The arc shown in Figures 12a and 12b moved slowly northward from thunderstorm activity near the Tampa Bay area. The region of the arc penetrated by the aircraft is shown in Figure 12d, which is a mesoanalysis based on the cloud field shown in Figure 12b. Notice how the amount of convection decreases along the arc during the 1-1/2 hours between Figures 12a and 12b and that no thunderstorms formed along the arc as it moved northward, although shower activity was

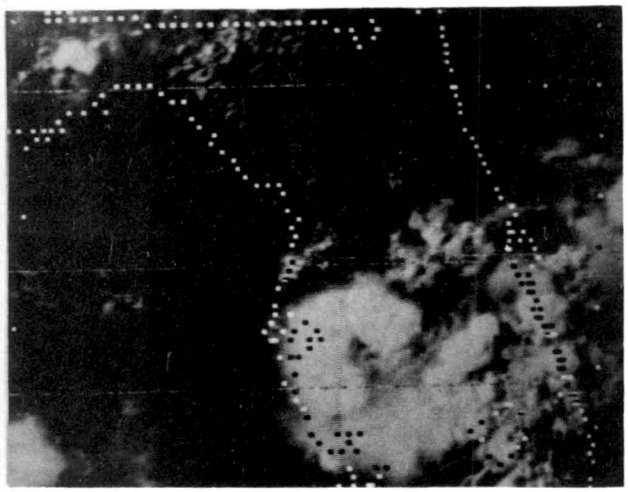

Fig 12a. 17 July 1980 at 2100 GMT.
GOES-East 1Km resolution visible image.

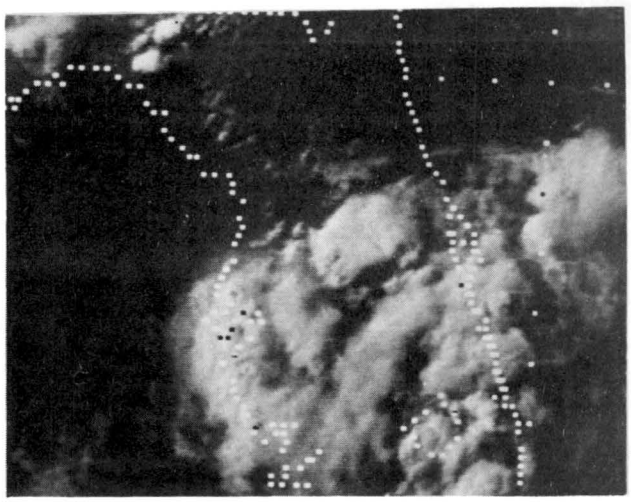

Fig 12b. 17 July 1980 at 2230 GMT.
GOES-East 1 Km resolution visible image.

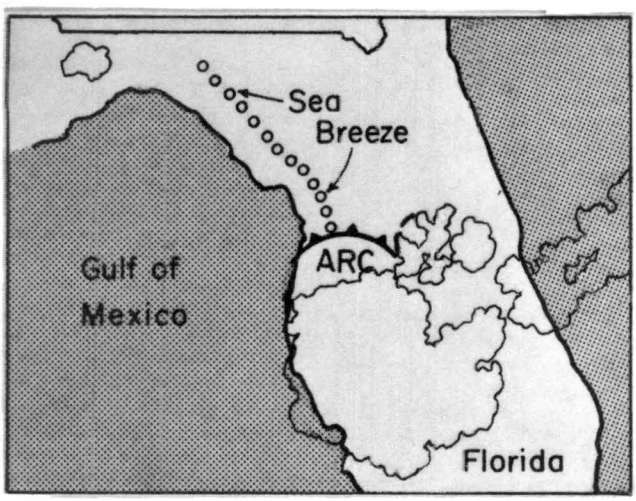

Fig 12c. Nephanalysis of Fig 12a.

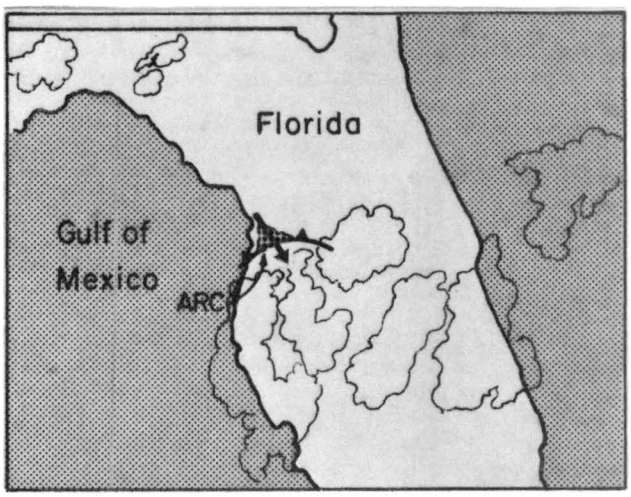

Fig 12d. Nephanalysis of Fig 12b. Arrow shows flight path, shaded area gives field of view for montage in Fig 12e.

Fig 12e. Montage of arc cloud region prior to penetration; note weak cumulus development.

observed during penetration near where the arc intersected the sea breeze front.

Figures 12c and 12d are mesoscale analyses of Figures 12a and 12b based on the cloud cover shown in those photographs, as well as analysis of animated frequent interval GOES imagery. The aircraft flight path is shown by the arrow in Figure 12d. Figure 12e, which was taken near the time of our penetration, shows the cloudiness associated with the arc shown in Figure 12b. Notice that this cloudiness is not as intense as that for the previous two cases.

The vertical velocity (w) and dew point (T_d) measurements show the typical warm, moist updraft region below cloud (arc line) base (Figure 13, pg. 34). The maximum updraft variations [$\Delta ( )_{max}$] of the three measured variables (T, T_d, w) from essentially constant environmental values are shown in Table 4 below.

Table 4. Maximum Variations of T, T_d and w for July 17, 1980 Arc Line Penetrations

$\Delta T_{max} = +0.7^{o}C$ to $-5^{o}C$

$\Delta T_{d}max = \pm 2.0^{o}C$

$\Delta w_{max} = +2.5$ m sec^{-1} to -1.5 m sec^{-1}

Again the vertical motion field appears to indicate typical descending motion on either side of the main updraft. This descending motion is not cooler than the main updraft core as was the case on 21 July 1980. Instead the sinking motion around the updraft is generally warmer and drier than the updraft air which itself is actually cooler and more moist than the environmental air at least 20 km from the updraft core (Figure 13). The relatively cool updraft core is interpreted as air that has overshot its equilibrium level and as a consequence appears cooler

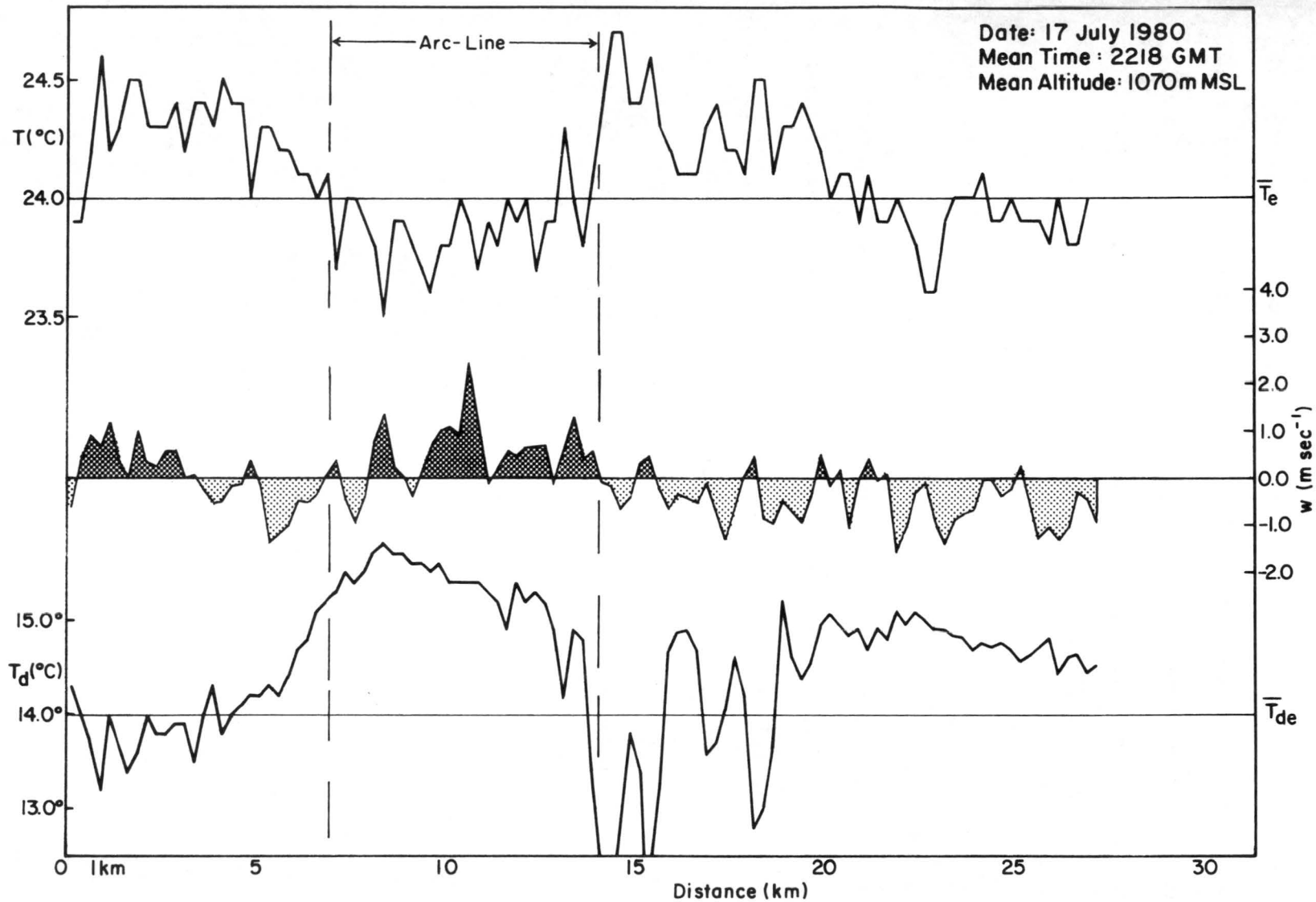

Figure 13. Aircraft Data of Arc Line Penetration for 17 July 1980, 2218 GMT.

The distribution of temperature (T), dew point (T_d), and vertical motion (w) are shown with respect to their mean environmental values: $\overline{T}_e$, $\overline{T}_{de}$, and w = o. The lateral boundaries of the cloud arc line are indicated by the dashed vertical lines at approximately ± 7 Km from the arc centerline.

than its environment. This phenomena, we believe, takes place when either the outflow weakens, the density surge line becomes stationary and well-mixed, and/or as the outflow advances into an airmass with marginal instability. During these dissipative stages, the weak lifting of marginal convectively unstable air along the arc line front does not necessarily initiate a positively buoyant updraft circulation to the cloud base level. That is, in the arc line dissipative stages, the small cumulus that appear are driven by a select number of updraft cores that have overshot their equilibrium level and are negatively buoyant when they condense at cloud base. Consequently, a relatively lower surface layer moisture content, marginal thermal instability, and/or weak lifting by the DSL frontal surface can all contribute to weak arc-line development as evidenced on this penetration.

In this particular case, the parent thunderstorm was more than 6 hours old with a weak and rather ill-defined, high cloud base arc line to its north. As a result, the warm, moist surface layer ahead of the weakened DSL was lifted as sporadic, small thermal elements that were well-mixed during their ascent to cloud base. However, primarily because of mixing and relatively low moisture content of the environment, many of these thermal elements reached an equilibrium level before they reached the condensation level. In this particular case, it appears that their equilibrium level was approximately 150 m below the penetration altitude of 1070 m MSL, while the cloud base exceeded 1250 m MSL. The flight level dew points were also somewhat lower on the 17th versus other measurement days where the cloud bases were somewhat lower.

IV. SUMMARY AND CONCLUSIONS

The importance of thunderstorm genesis along storm outflow boundaries (i.e., arc cloud lines) has been well documented from satellite imagery (Parker and Hickey, 1980; Purdom, 1973, 1982) and from other more conventional observations (Magor, 1959; Miller, 1972). What has not been documented in detail is the temperature, moisture and air motion features of the arc line, sub-cloud region, and the leading edge (DSL) of the outflow boundary. We have presented here what we believe to be the first measurements and analyses of the arc cloud line's structure in the layer below cloud base but above the DSL.

4.1. Arc Cloud Line Life Cycle

The individual cases include developing, mature and dissipating stages of the arc line lifecycle. The results, although based on a minimum number of samples, appear to indicate the following:

(1) Arc Line Developing Stage:

The developing stage of the arc line life cycle may be characterized by a relatively rapidly moving DSL. This promotes the most intense mixing at the DSL boundary and the largest values of vertical motion and temperature excess in the updraft region above the DSL (Figure 7). The strong mixing may also result in dry air intrusion by the relatively cool, dry outflow air into the warmer and more moist marine air that is thrust upward by the forward motion of the DSL (Figure 10). Similar turbulent mixing features are exhibited by laboratory gravity currents and low-level atmospheric observations of haboobs, squall lines and cold fronts. These observations suggest that intense mixing may also take place along the arc line DSL which supports the dry air intrusion

hypothesis. This stage is most closely represented by the 22 July 1982 case.

(2) Arc Line Mature Stage:

In the mature stage, the DSL is well established and moves out from the parent storm at a more uniform velocity than that exhibited during the developing stage. The updraft region that develops above the DSL and which feeds the arc line clouds is characterized by a warm, moist and positively buoyant updraft core (Figure 5). This stage is represented by the 21 July 1982 case. Both stages (1) and (2) indicate the presence of a return flow ($w < 0$) around the main updraft core.

(3) Arc Line Dissipation Stage:

The dissipation stage of the arc line life cycle is characterized by little or no motion of the DSL. This results in relatively weak updraft cores below the stagnant or dissipating cloud arc line. In some cases, these updraft regions may become negatively buoyant below cloud base (Figure 13). While these updraft cores may be mechanically (inertially) driven beyond their equilibrium levels, they may not reach the higher than normal cloud base levels. This stage is possibly represented by the 17 July 1980 case where the outflow and the DSL were weakly connected with the parent storm which was approximately 6 hours old and itself in its dissipation stage.

4.2. Arc Cloud Lines and New Convective Development

From our measurements and observations, we draw the following conclusions concerning the importance of arc cloud lines in the development and evolution of deep convection. In the undisturbed convective environment in advance of the arc cloud line, small buoyant

thermals rise from the surface boundary layer and rapidly mix with the surrounding environment. Because of their size, lack of organization and rapid mixing, they are unable to sustain an updraft core and in most cases never reach the condensation level - a few produce short-lived fair weather cumulus. However, as the outflow moves away from its parent thunderstorm, mechanical lifting occurs creating a new local environment in the vicinity of the density surge line. This new local environment is much more favorable for the growth of convective elements because of its organization, size and stronger vertical motion. Thus the mechanical lifting of the relatively warm, moist environmental air by the leading edge of the storm's outflow leads to the development of a warm buoyant updraft above the DSL which initiates the development of the"arc cloud line".

Rain showers were observed beneath some of the cumulus congestus along the arc cloud lines. This precipitation/evaporation process, and the production of negatively buoyant air in the boundary layer, is important in the continuous regeneration of convective clouds along arc cloud lines. Furthermore, horizontal divergence of the relatively cool, low-level, outflow air mass promotes sinking of the air above it. This in part accounts for the relatively clear skies and stable cloud forms we observed in the interior portions of the arcs.

In our flights we purposely avoided regions of arc cloud line merger with highly convective areas (towering cumulus or thunderstorms) as well as areas of intersection between two arc cloud lines. This procedure was followed for safety purposes since such areas are noted for rapid thunderstorm development. At this point we can only hypothesize why such regions are highly favored for more intense development.

(1) Merger is defined to occur when an arc cloud line moves into a region of pre-existing cumulus and cumulus congestus cloudiness. Such areas differ from the undisturbed convective environment in that they already exhibit some amount of organization and realized instability. Such an environment is able to utilize the organization and forcing of the arc cloud line much more effectively than the undisturbed environment. Thus, the convection that forms along an arc as it moves into a pre-existing convective area often reaches the cumulonimbus stage.

(2) Intersection is defined to occur when two arc cloud lines come into direct contact. As the two arc cloud lines approach one another, increasing convergence between them results in a deeper moist layer. As two arc cloud lines intersect, a greater degree of organization and stronger forcing of the boundary layer's vertical motion field occurs (as compared to a single arc cloud line). This causes the development of a highly organized and strong buoyant updraft at the location of the intersection. It is the formation of these highly organized and strong buoyant updrafts that lead to the development of intense thunderstorms at points of arc cloud line intersection.

4.3 Experiment Operation

Accurate vectoring of the aircraft to areas of arc cloud line activity would have been impossible without the use of real-time GOES imagery. In addition, the high mobility of the aircraft allowed multiple level penetrations of arc cloud lines at the desired time and location selected by the on-board scientists. These measurements and operational capabilities provide distinct advantages over fixed tower measurements.

In analyzing results from experiments of this type, the use of rapid scan GOES imagery is essential. These image data sets permit the

accurate definition of the arc cloud line(s) that correspond to the aircraft measurements at a particular time and location.

V. FUTURE RESEARCH

In order to complete a descriptive model of the arc cloud line structure, our initial field measurement effort requires considerable expansion in both the time and space domains. For example, more measurements are needed to:

(1) define the low-level boundary layer structure and life cycle of the density surge line (DSL) associated with arc cloud lines;

(2) relate the intensity of the outflow to the parent storm cloud features deduced from radar and/or satellite observations;

(3) investigate the relative importance of the turbulent mixing hypothesis suggested by the laboratory gravity current tank experiments and by other similar atmospheric flow phenomena;

(4) develop a detailed thunderstorm outflow model that explains the salient structural features of the arc cloud line as well as its time evolution. The predictive capability appears feasible once a sufficient data set is accumulated which adequately describes the development as well as the dissipative stages of the cloud arc-line life cycle.

The results of this research should be extremely useful in forecasts of new severe storm development deduced from satellite observations. In addition, information concerning the turbulence and wind shear structure near and within the outflow boundaries will be of critical importance to military and civilian aircraft operations as well as space shuttle landing operations.

VI. ACKNOWLEDGMENTS

The research work in this report was supported by NOAA/NESS Grant NA80AA-D-00056.

The authors wish to thank NESS meteorologists Vince Oliver and Ray Zehr and those at the Kansas City SFSS for their expert advice concerning the selection penetration areas. Special thanks to Ms. Joanne Williams for preparation of the manuscript and Duayne Barnhart for expert photographic support.

A portion of the computer support for reduction of aircraft data tapes was provided by NCAR.

VII. REFERENCES

Barnes, S.L. (Ed.), SESAME 1979 Data User's Guide. NOAA/ERL, U.S. Department of Commerce, Boulder, CO, 236 pp.

Brandes, E.A. 1978: Mesocyclone evolution and tornadogenesis: Some observations. Mon. Wea. Rev. 106, 995-1101.

Charba, J., 1974: Application of gravity current model to analysis of squall-line gust front. Mon. Wea. Rev., 102, 140-156.

Delsi, M., 1968: Downdraft haboob in Khartoum, Sudan. Met. Dept., Khartoum, 14 pp.

Fankhauser, J., 1971: Thunderstorm-environment determined from aircraft and radar observations. Mon. Wea. Rev., 99, 171-192.

Fankhauser, J., 1976: Structure of an evolving hail storm, part II: Thermodynamic structure and airflow in the near environment. Mon. Wea. Rev., 104, 576-587.

Goff, C.R., 1976: Vertical structure of thunderstorm outflows. Mon. Wea. Rev., 104, 1429-1440.

Idso, S.B., R.S. Ingram, and J.M. Pritchard, 1972: An American haboob. Bull. Amer. Meteor. Soc., 53, 930-935.

Keulegan, G.H., 1957: An experiment study of the motion of saline water from locks into fresh water channels. 13th Progress Report on Model Laws for Density Currents, U.S. Nat. Bur. Standards, NO 5168.

Keulegan, G.H., 1958: The motion of saline fronts in still water. 12th Progress Report on Model Laws for Density Currents, U.S. Nat. Bur. Standards, NO. 5831.

Lawson, T.J., 1971: Haboob structure at Khartoum. Weather, 26, 105-112.

Leverson, V.H., P.C. Sinclair, J.H. Golden, 1975: Waterspout wind, temperature and pressure structure deduced from aircraft measurements. Ninth Conf. Sev. Local Storms, Oct. 21-23, Norman, OK, AMS, Boston, MA.

Lilly, K.K. (ed.), 1977: Project SESAME: Planning documentation volume. NOAA/ERL, U.S. Department of Commerce, Boulder, CO, 308 pp.

Maddox, R.A., 1980: Mesoscale convective complexes. Bull. Am. Met. Soc., 61, 1374-1387.

Magor, B.W., 1959: Mesoanalysis: Some operational analysis techniques utilized in tornado forecasting. Bull. Am. Met. Soc., 40, 499-511.

Martin, H.C., 1973: Some observations of the microstructure of dry cold fronts. J. Appl. Meteor., 12, 658-663.

Middleton, G.V., 1966: Experiments on density and turbidity currents, I. Motion of the head. Canadian J. Earth Sci., 3, 523-546.

Miller, R.C., 1972: Notes on analysis and severe-storm forecasting procedures of the Air Force Global Weather Central. AWS Technical Report 200 (rev), Air Weather Service (MAC), U.S. Air Force, 190 pp.

Parker, W.T., and R.D. Hickey, 1980: The Cheyenne tornado of 16 July 1979. Nat. Wea. Digest, 5, 45-62.

Purdom, J.F.W., 1973: Meso-highs and satellite imagery. Mon. Wea. Rev., 101, 180-181.

Purdom, J.F.W., 1976: Some uses of high-resolution GOES imagery in the mesoscale forecasting of convection and its behavior. Mon. Wea. Rev., 104, 1474-1483.

Purdom, J.F.W., 1979: The development and evolution of deep convection. Preprints 11th Conference on Severe Local Storms, Kansas City, MO, AMS, Boston, MA, 143-150.

Purdom, J.F.W., 1982: "Chapter 3.1, Subjective Interpretation of Geostationary Satellite Data for Nowcasting." Nowcasting, K.A. Browning (Ed.), Academic Press Inc., London, 256 pp.

Purdom, J.F.W. and Marcus, K, 1982: Thunderstorm trigger mechanisms over the southeast United States. Preprints 12th Conference on Severe Local Storms, San Antonio, TX, AMS, Boston, MA, 487-488.

Simpson, J.E., 1969: A comparison between laboratory and atmospheric density currents. Quart. J. R. Met. Soc., 95, 758-765.

Simpson, J.E., 1972: Effects of the lower boundary on the head of a gravity current. J. Fluid Mech., 53, 759-768.

Simpson, J.S., 1980: Downdrafts as linkages in dynamic cumulus seeding effects. J. Appl. Meteor., 19, 477-487.

Simpson, J.S. and Dennis, A.S., 1974: " Cumulus clouds and their modification." Weather Modification, W.N. Hess (Ed.), Wiley, New York, 229-280.

Sinclair, P.C., 1973: Severe storm air velocity and temperature structure deduced from penetrating aircraft. 8th Conf. on Sev. Local Storms, Oct. 15-17, AMS, Boston, MA.

Sinclair, P.C., 1974: Vertical transport of desert particulates by dust devils and clear thermals. Proc. Atmospheric-Surface Exchange of Particulates and Gaseous Pollutants, Richland, Atomic Energy Commission, 497-527.

APPENDIX A

Cessna Turbo 207 Atmospheric Research Aircraft

Over the past 16 years we have developed a number of Airborne Atmospheric Data Systems (AADS-1A to 5A) for the direct measurements of the three-dimensional velocity field, temperature, dew point, pressure, atmospheric gases and particulates, etc. These systems have been specially designed for various aircraft (McDonnell F-101B, Lockheed T-33, North American T-6 and T-28, Beech Queen Air, Cessna T207, Shinn 2150A, and a Laister Kaufmann sailplane) for measurements in atmospheric systems ranging from mesoscale systems and severe thunderstorms to waterspouts and dust devils (Sinclair 1966, 1969, 1973, 1974a, b, 1977, 1978a, b, 1979, 1982a, b, c, 1983). A miniaturization of these previous systems has been designed and constructed for the Cessna T207 aircraft (Figs. 2 and 3). It is believed that this is the first installation of this type on a light single-engine aircraft.

The gust velocity measurement system is designed so as to be independent of the aircraft sensitivity to atmospheric motions and/or pilot induced motions. The measurement technique (Sinclair 1969, 1973) requires knowledge of the motion of the air relative to the airplane ($V_{p,g}$) in order to calculate the atmospheric motion with respect to the ground ($V_{a,g}$) i.e.,

$$\mathbf{V}_{a,g} = \mathbf{V}_{a,p} + \mathbf{V}_{p,g}$$

which for the vertical component ($w_{a,g}$) can be expressed as (Fig. 1).

$$w_{a,g} = \mathbf{K} \cdot \mathbf{V}_{a,g} = w_{a,p} + w_{p,g}$$

The vertical component of the air relative to the aircraft ($w_{a,p}$) can be cxpressed as:

$$w_{a,p} = -V_{a,p} \sin \gamma$$

or

$$w_{a,p} = V_T \sin(\alpha_z - \theta) = V_T (\sin\alpha_z \cos\theta - \sin\theta \cos\alpha_z)$$

where V_T is the true airspeed ($V_T = -V_{a,p}$), and the flight path angle, γ, is

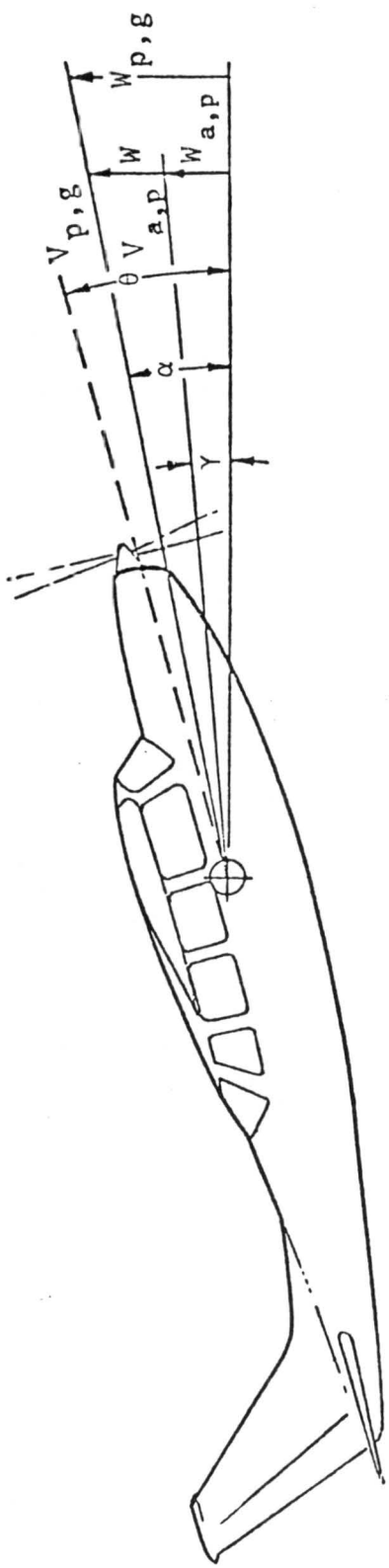

Fig. 1: Relationship of vertical velocity measurement system and flight axes.

Fig. 2: Cessna Turbo 207 Atmospheric Research Aircraft.

The Cessna T207 aircraft is the largest single-engine light plane manufactured in the U.S. and consequently it provides maximum volume and payload capabilities at minimum cost. The aircraft is STOL equipped for high accuracy wind and gust measurements and isokinetic air sampling requirements. The gust probe system is mounted in a pod under the left wing and a doppler navigation - wind system is located in a specially designed pod located on the bottom of the fuselage near the tail of the aircraft.

A fast response total temperature sensor is shown mounted on the upper part of the vertical plate on the right wingtip. On the lower part of the plate, a special splitter plate mount houses the Cambridge dew point sensor. The splitter plate provides unobstructed flow past the sensor air ports. The temperature and dew point sensors are mounted on the wingtip to minimize engine effects and contamination and adverse airflow situations at other wing-fuselage locations.

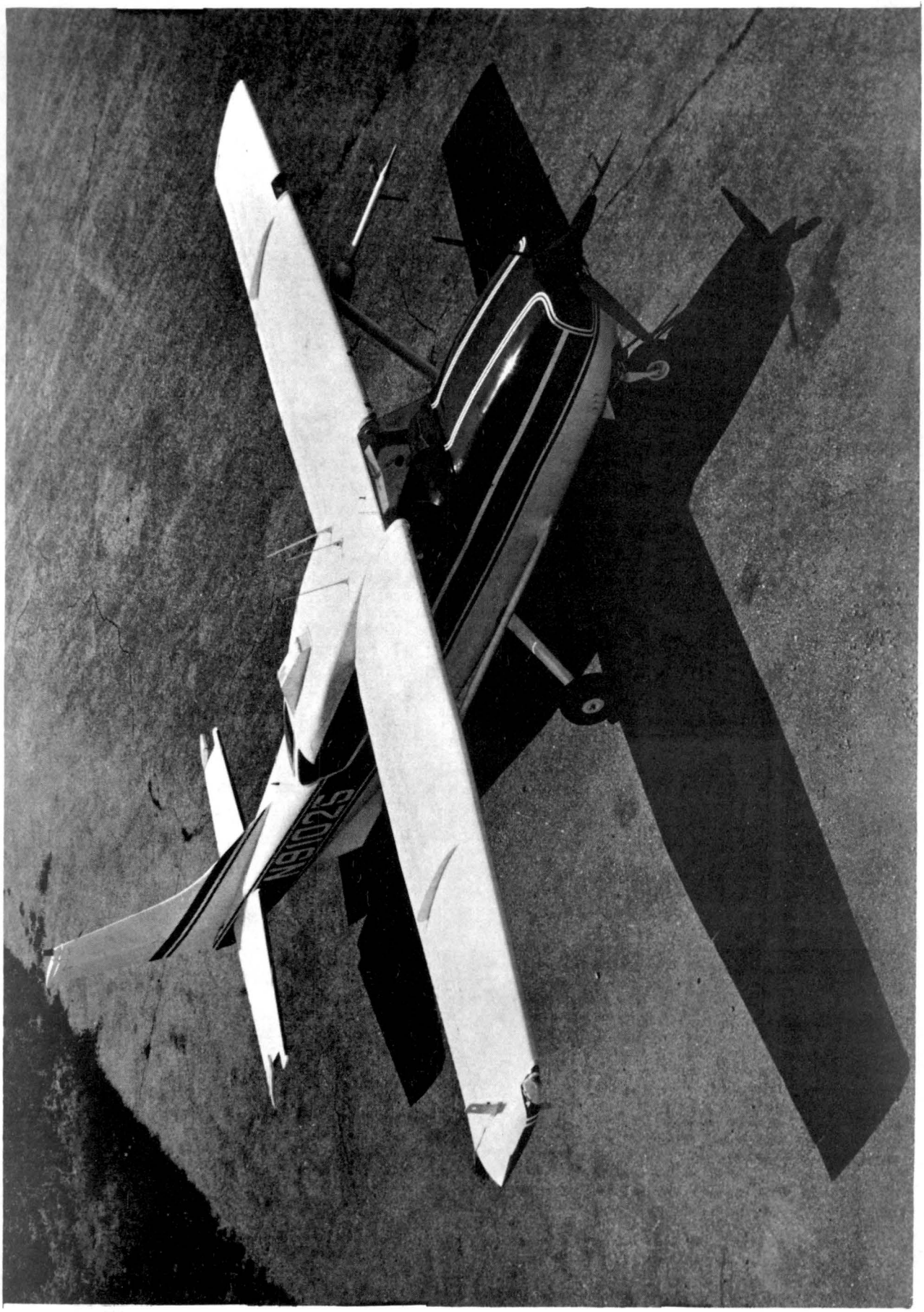
N9025

Fig. 3: Cessna T207 Gust Probe and Gyro Reference System.

The gust probe boom contains the two gust vanes (α and β vanes) and the pitot static tube. The specially designed gyro reference system is located in the streamlined fiber-glass pod attached to the underside of the left wing. Total weight of the system is less than 45 lbs. The APN-153V doppler wind system located in a pod on the belly of the aircraft near the tail is a four beam, Janus type doppler wind system. It provides the pilot with continuous read-out of ground speed and drift angle - these values along with airspeed and heading are recorded on an airborne digital magnetic tape recorder. The streamline housing is constructed of aluminum and fiber-glass so as to provide a mount for a special radome below the fully enclosed pitch compensated antenna. This is the first time that such an installation has been made on a light, single-engine aircraft.


N91025

related to the pitch angle, θ, the angle of attack, α, by $\gamma = \gamma_z - \theta$. Note α_z refers to the angle of attack measured in earth coordinates - the angle of attack (α) measured in aircraft coordinates is related to α_z through the aircraft roll angle (ϕ).

The aircraft vertical velocity ($w_{p,g}$) is obtained by integration of the vertical component of the acceleration (a_z). The vertical motion of the air with respect to the ground is then given by:

$$w_{a,g} = V_T (\sin\alpha_z \cos\theta - \sin\theta \cos\alpha_z) + \int_o^t a_z dt - w_{p,g}(o)$$

where $w_{p,g}(o)$ is the vertical velocity of the aircraft at time $t = 0$. The angle of attack (α_z) measured in earth coordinates is related to the angle of attack (α) measured in aircraft coordinates by:

$$\sin\alpha_z = \sin\alpha \cos\phi + \sin\beta \sin\phi$$

where ϕ and β are the aircraft roll angles and yaw angles, respectively. Under the assumption that the angles: α, β, and θ are small, the expression for $w_{a,g}$ can be simplified to:

$$w_{a,g} = V_T\alpha + V_T\beta\phi - V_T\theta + \int_o^t a_z dt - w_{p,g}(o) + L\dot{\theta}$$

For angles less than 10 degrees, the small angle assumption results in an error in the computed $w_{a,g}$ of less than 2%, which is normally less than the measurement capabilities of the system. The additional term ($L\dot{\theta}$) is necessary if the accelerations are measured at a location other than at the point where the angles are measured. For example, if the accelerations are measured at the c.g. of the aircraft, then the pitch rate ($\dot{\theta}$) must be multiplied by the distance (L) between the accelerometer and the measurement point of α in order to take into account the aircraft pitching velocity in the determination of

$w_{a,g}$. The expressions for the longitudinal ($u_{a,p}$) and lateral ($v_{a,p}$) velocity components are slightly more complicated than the vertical component, but they are obtained by a similar analysis, i.e., utilizing the small angle approximation:

$$u_{a,g} = -V_T\,[\sin\psi + \beta(\cos\psi + \theta\phi\,\sin\psi) + \alpha(\theta\sin\psi - \phi\cos\psi)] + u_{p,g} - L(\dot{\theta}\theta\sin\psi - \dot{\psi}\cos\psi)$$

$$v_{a,g} = -V_T\,[\cos\psi - \beta(\sin\psi - \theta\phi\cos\psi) + \alpha(\theta\cos\psi + \phi\sin\psi)] + v_{p,g} - L(\dot{\psi}\sin\psi + \dot{\theta}\theta\cos\psi)$$

where ψ is the heading angle measured from true north. The ground speed components $u_{p,g}$ and $v_{p,g}$ are obtained from the doppler wind system.

It is apparent that several independent measurements are needed in order to evalutate the vertical motion ($w_{a,g}$). Measurements of α and β are made with lightweight, but durable flow vanes. The flow vanes and pitot system are mounted on a nose-boom sufficiently far in front of the aircraft wing to minimize upwash and pressure effects associated with the aircraft induced flow fields. As in all boom-vane designs, the length of the boom is always a compromise between boom natural frequency, size, structural integrity, and complete removal of upwash and pressure errors. The boom natural frequency requirement of 12 cps and the available aircraft mounting location specified the boom size. Upwash and static pressure errors have been removed by careful tower fly-by calibrations and aircraft intercomparison flight tests. Dynamic response characteristics of the vane-pitot tube system were accomplished by programmed pitch-roll flight tests (roller-coaster maneuvers). These calibrations and flight tests indicate that the AADS-5B system has the following mean difference error bands:

$$\Delta u = \Delta v = \Delta w = \pm 0.5 \text{msec}^{-1};\ \Delta T = \pm 0.3°C;\ \Delta P = \pm 0.005 \text{ psi}$$

pitch (θ), pitch rate ($\dot{\theta}$), roll (ϕ), roll rate ($\dot{\phi}$), yaw (β), and heading

(ψ) angles or angular rates are measured by a strapped-down gyro reference system. The vertical velocity of the aircraft ($\int_0^t a\,dt$) is obtained from a three-axis accelerometer system located at the aircraft center-of-gravity (c.g.). Because the recorded aircraft c.g. accelerations contain accelerometer errors which tend to be additive during the integration, the calculated vertical velocities may contain significant errors after approximately one minute of operation. To minimize these errors as much as possible during the flight profile, the measured pressure altitude variations are used to correct the vertical accelerometer calculations. The true airspeed is calculated from measurements of total pressure, static pressure and total temperature. The static temperature and true airspeed are determined by use of the compressible, sub-sonic flow equations:

$$\frac{P_t - P_s}{P_s} = \left(1 + \frac{\gamma-1}{2} M^2\right)^{\frac{\gamma}{\gamma-1}} - 1$$

$$\frac{T_t}{T_s} = 1 + \frac{\gamma-1}{2} \xi M^2$$

$$V_t = T_t^{1/2} \left\{gR/\left(1 + \frac{\gamma-1}{2}\right)\right\}^{1/2}$$

where

P_t = total or ram pressure

P_s = static pressure

M = Mach number

T_t = total temperature

T_s = static temperature

ξ = recovery factor

γ = ratio of specific heats of air; c_p/c_v

V_t = true airspeed

Relatively fine structure of the turbulent velocity spectrum (0.04 to 10 cycles sec^{-1}) can be obtained from the data which is recorded on a 1000 character per second, digital, incremental magnetic tape recorder. The fast response sensors are sampled every 0.02 sec while the slower responding instruments are sampled every 0.04 sec. Eight-pole Butterworth filters are used to remove data fluctuations with frequencies higher than 10 cps. This provides an effective filter system for removing boom vibration errors and electronic noise.

The entire gust probe system is mounted below the left wing of the aircraft in a modified drone tip tank (Fig. 3). The α - β vane system and pitot tube are located at the front of the instrumentation boom which extends from the nose of the tip tank to a point ahead of the wing and the plane of the propellor. All of the gust vane electronics as well as the pressure transducers and gyros are rigidly fastened to the boom structure inside the drone tip tank.

In addition to the gust velocity (u', v', w') measurement system, an on-board doppler wind system (APN-153V) provides accurate measurements of ground speed and aircraft drift angle. These data, along with aircraft heading and true airspeed provide mean (5 sec avg.) horizontal wind componenets $(\overline{u}, \overline{v})$. Precise flight tracks over the ground can be programmed into the doppler computer to satisfy a wide variety of measurement requirements. The dew point and the total temperature are also continuously recorded with the other parameter at a sampling rate of 0.04 sec (the gust vanes are fast sampled at 0.02 sec). The measurement locations are obtained continuously from LORAN-C ($\pm$ 70 m), VOR-DME ($<\pm 10^3$ m), and/or doppler navigation coordinates ($<\pm$ 500 m relative).

The T207 research aircraft with the AADS-5A system is therefore capable of not only flight testing the IR LLWS prediction system but it also provides detailed air motion and state parameter data which is required to quantitatively validate the sensitivity and response of the IR spectral ranging system under a wide variety of wind shear situations. In addition, the low flight speeds ($\sim$ 50 m sec $^{-1}$) of the T207 and the high speed recording (0.02-0.04 sec) of the AADS-5A measurement system will provide greater space-time resolution of the flight test data then has been possible in the past.

References

Sinclair, P.C., 1966: A quantitative analysis of the dust devil. Ph.D. dissertation, Univ. of Arizona, 292 pp.

Sinclair, P.C., 1969: Vertical motion and temperature structure of severe convective storms. Preprints Sixth Conference Thunderstorm Phenomena, Severe Local Storms, Apr. 8-10, Chicago, Amer. Meteor. Soc., 346-350.

Sinclair, P.C., 1973: Severe storm air velocity and temperature structure deduced fro penetrating aircraft. Preprints Eighth Conf. Severe Local Storms, Denver, Amer. Meteor. Soc., Oct. 15-17, 25-32.

Sinclair, P.C., 1974a: Severe storm turbulent energy structure. Preprints Sixth Conf. Aerospace and Aeronautical Meteorology. El Paso, Amer. Meteor. Soc., Nov. 12-14, 13 pp.

Sinclair, P.C., 1974b: Vertical transport of desert particllates by dust devils and clear thermals. Proc. Atmosphere-Surface Exchange of Particulates and Gaseous Pollutants, Richland, Atomic Energy Comm., 497-527.

Sinclair, P.C., et al, 1977: The vortex structure of dust devils, waterspouts, and tornadoes. Tenth Conf. Severe Local Storms, Omaha, Amer. Meteor. Soc., Oct. 18-21.

Sinclair, P.C., 1978a: Velocity and temperature structure near and within severe storms. Final Report, NOAA/NSSL, Norman, OK.

Sinclair, P.C., 1978b: Vortex structure and dynamics of Florida Keys waterspouts. Final Report, NOAA/ERL, Boulder, CO.

Sinclair, P.C., 1979: The removal and transport of desert particulates by dust devils. Final Report to the Lawrence Livermore Laboratory, University of California Atomic Energy Commission.

Sinclair, P.C., 1982a: Integration of research aircraft data and 3 minute interval GOES data to study the genesis and development of deep convective storms. Preprints Twelfth Conv. Severe Local Storms, San Antonio, Amer. Meteor. Soc., January.

Sinclair, P.C., 1982b: Puff transport and diffusion experiment. Final Report: Phase I & II, Savannah River Laboratories, E.I. duPont de Nemours Inc.

Sinclair, P.C., 1982c: Aircraft measurements and analysis of severe storms. Final Report, NASA.

Sinclair, P.C., J.F.W. Purdom, 1983: Shuttle recovery requirements and the development of arc cloud lines from thunderstorm outflows. Ninth Conf. on Aerospace and Aeronautical Meteor, June 6-9, Omaha, NB.